To the Graduate Council:

I am submitting herewith a thesis written by Stephen Webster Kennerly entitled "The Scattering and Absorption of Light Due to Surface Resonances on Submicron Oblate Spheroidal Particulates." I have examined the final copy of this thesis for form and content and recommend that it be accepted in partial fulfillment of the requirements for the degree of Master of Science, with a major in Physics.

Thomas L. Ferrell, Major Professor

We have read this thesis and recommend its acceptance:

Accepted for the Council:

The Graduate School

THE SCATTERING AND ABSORPTION OF LIGHT DUE TO SURFACE RESONANCES ON SUBMICRON OBLATE SPHEROIDAL PARTICULATES

A Thesis

Presented for the

Master of Science

Degree

The University of Tennessee, Knoxville

Stephen Webster Kennerly

December 1983

DEDICATION

To my wife Terri, for her endless love, support and encouragement and to Mother and Dad for providing love when I needed it and for pushing me to succeed when I needed it most and wanted it the least.

ACKNOWLEDGMENTS

The author would like to express his gratitude for the guidance and financial support given him by Dr. Thomas L. Ferrell throughout this work. A special expression of gratitude is given to Dr. John W. Little for untold amounts of experimental and theoretical assistance.

The assistance of the Health and Safety Research Division of Oak Ridge National Laboratory in providing laboratory and computing facilities and to The University of Tennessee, Knoxville, Physics Department for financial support is gratefully acknowledged.

A special thanks is given to Dr. K. C. Mamola for his guidance and instruction during the early years of the author's physics education.

Another special thanks is given now to Ms. Maxine Martin whose typing skills and knowledge shall enable the author to tiptoe through the treacherous tulip garden of the Graduate School.

At last, the author expresses his indebtedness to his many colleagues and friends for their support, especially in maintaining a sense of humor throughout this ordeal.

ABSTRACT

The experimental part of this thesis consists of measuring the optical absorbance of a collection of silver oblate spheroidal particulates as a function of wavelength, polarization, and angle of incidence. The method of producing such a collection is described along with measuring a few of the important characteristics like particle size, separation, and density. The experimental data are then compared with theoretical absorbances calculated using scattering and absorption cross sections. The cross sections are derived using a dipole approximation.

TABLE OF CONTENTS

LIST OF FIGURES

CHAPTER I

INTRODUCTION AND HISTORY

Man's curiosity about the scattering and/or absorption of light seems to have never been totally satisfied. This is evidenced by the enormous amount of published literature on the subject.

One of the first scientists to study such phenomena, and probably the most famous, was Lord Rayleigh. He published several papers concerning the scattering of light, which he referred to as "electricity waves." In one investigation, Rayleigh studied the scattering of light by small metal spheres and ellipsoids [1.1] which was the earliest work related to the present investigation. Rayleigh also solved analogous problems from acoustics using the mathematical formalism for waves.

Many investigators followed the work of Lord Rayleigh. J. C. Maxwell-Garnett published an often cited paper [1.2] concerning the absorption by small metal spheres embedded in glasses. This paper showed that certain regions of the spectrum were preferentially absorbed by the metal particulates, thereby giving the glasses a distinct color as viewed in transmission. G. Mie worked extensively on scattering and developed a great deal of the theoretical formalism for the scattering of light by spheres [1.3]. Following the work of Mie, V. R. Gans published works on the scattering of light by objects with spheroidal geometries [1.4]. In 1939, experimental work on the optical properties of thin metal films [1.5] was done by Erwin David.

He was the first to postulate the existence of disk-like metal particles in thin metal films.

Beginning in the early 1960's, there seemed to be an increased interest in the optical properties of thin discontinuous films of metals. Shigeo Yamaguchi, in 1962, published the results of optical transmission measurements [1.6] made, as a function of angle of incidence and polarization, on thin heat-treated silver films. His heat treatment consisted of allowing the silver films to remain under vacuum while heating the films to approximately 200°C. Yamaguchi, from the results of his measurements, postulated that his films were either roughened or broken apart during the heat treatment. In 1967, N. Emeric and A. Emeric published the results of optical transmission measurements [1.7] made upon thin silver films. The measurements displayed a definite angular dependence as well as the usual polarization dependence. They qualitatively attributed the angular dependence to the presence of ellipsoidal particles in the film. However, very little was done to quantitatively relate the angular dependence to the particle shape. The next year, D. C. Skillman and C. R. Berry measured the optical absorbance of gelatins containing silver prolate spheroids [1.8]. This paper contained electron micrographs of the particles in the gelatin. The micrographs definitely revealed the prolate shape of the silver particles. Their measurements revealed two absorbance peaks corresponding to dipole oscillations along the minor and major axes.

In the present work, optical absorbance measurements were made on oblate rather than prolate silver spheroids. The difference being that prolate particles are shaped somewhat like an elongated watermelon while the oblate particles take on a shape similar to that of a door-knob. In the work by Skillman and Berry the spheroids' minor and major axes were randomly oriented so that two absorbance peaks were always present. This is not the case in the present investigation. Here, most of the spheroids are aligned such that their minor axes are parallel. This gives rise to an angular dependence in the absorbance similar to that observed by Emeric and Emeric.

In an effort to quantify the shape dependence of the absorbance of silver particles, oblate spheroidal coordinates have been employed in the theoretical part of this thesis. These coordinates may be directly related to the minor-to-major axis ratio, which is a more intuitive measurement of the shape. The theoretical absorbances, calculated from the dipole scattering and absorption cross sections, are compared with favorable results to experimental absorbance measurements.

Much of the motivation for the present work is due to recent measurements of radiative emission from silver spheroids excited by electron bombardment [1.9]. In that work, the theoretical development was quantum mechanical while the present work employs a purely classical approach.

CHAPTER II

THEORY

In this chapter, the theoretical formalism is developed in some detail from first principles. First, a discussion of oblate spheroidal coordinates is presented. This is followed by a discussion of the solutions to Laplace's equation in oblate spheroidal coordinates. The solutions are then applied to the problem of dielectric oblate spheroid in a uniform, but time varying, electric field. From the solution to this problem, expressions for the potential (both inside and outside the spheroid), surface charge density, induced dipole moments, and polarizability are found. After this, the time averaged Poynting vector is used in calculating expressions for the absorption and scattering cross sections in the dipole approximation. The expressions for the cross sections are analyzed in Section D to identify the main factors affecting the cross sections. In the final section, it is shown that, in the limiting case of a sphere, expressions for the polarizabilities converge to the spherical polarizability.

A. OBLATE SPHEROIDAL COORDINATES

The coordinate system of interest here is oblate spheroidal coordinates [2.1]. The three families of mutually orthogonal surfaces associated with the coordinate system are confocal ellipsoids, single-sheeted hyperboloids and half planes. They are illustrated in a cross section given in Figure 2-1.

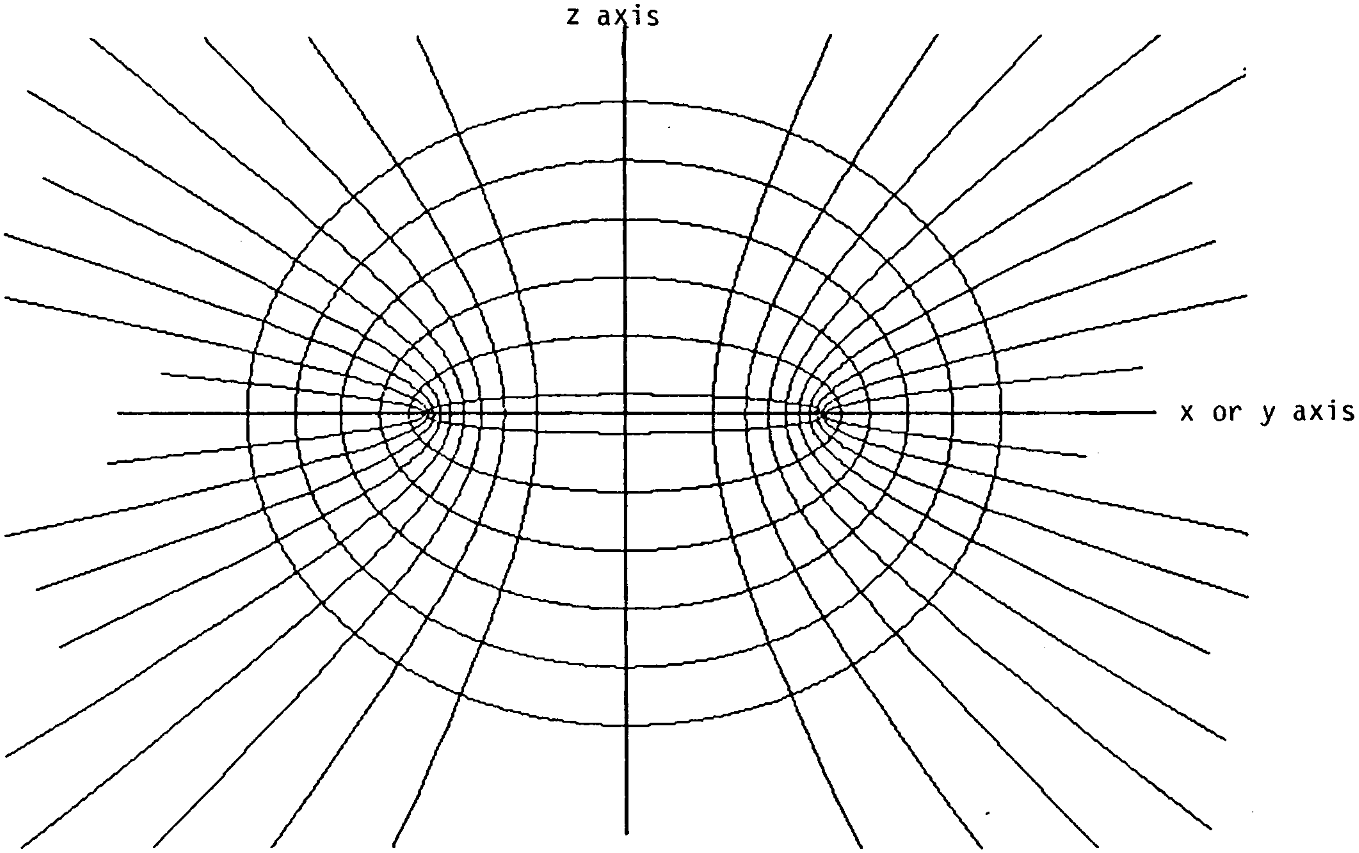

Figure 2-1. Cross section of oblate spheroidal coordinates. The three dimensional system is formed by rotating the cross section about the z-axis.

The family of ellipsoids is generated by

$$\frac{x^2 + y^2}{1 + \eta^2} + \frac{z^2}{\eta^2} = a^2 \qquad (2\text{-}1)$$

where a is the focal length. One can see that an ellipsoid can be generated by holding the value of η constant and that an entire family is generated by various values of η. Here, η may take on all non-negative values ($0 < \eta < \infty$).

The family of single sheeted hyperboloids is generated by

$$\frac{x^2 + y^2}{1 - \mu^2} - \frac{z^2}{\mu^2} = a^2 \qquad (2\text{-}2)$$

where a again is the focal length and $\mu = \cos \beta$, with β being the angle which the asymptote of each hyperboloid makes with the z-axis. One can also see that a single sheeted hyperboloid can be generated by holding the value of μ constant. The various values of μ generate confocal single sheeted hyperboloids that are orthogonal to the surfaces generated by Eq. (2-1). The range of μ is given as $-1 \leq \mu \leq +1$.

In Figure 2-1, a two-dimensional diagram [2.2] was constructed that showed a series of confocal ellipses and hyperbolas. The three-dimensional system is formed by rotation about the z axis. In Figure 2-2, just the family of ellipses is shown along with the corresponding values of η for each ellipse. Figure 2-3 is the family of hyperbolas with the corresponding values of μ shown.

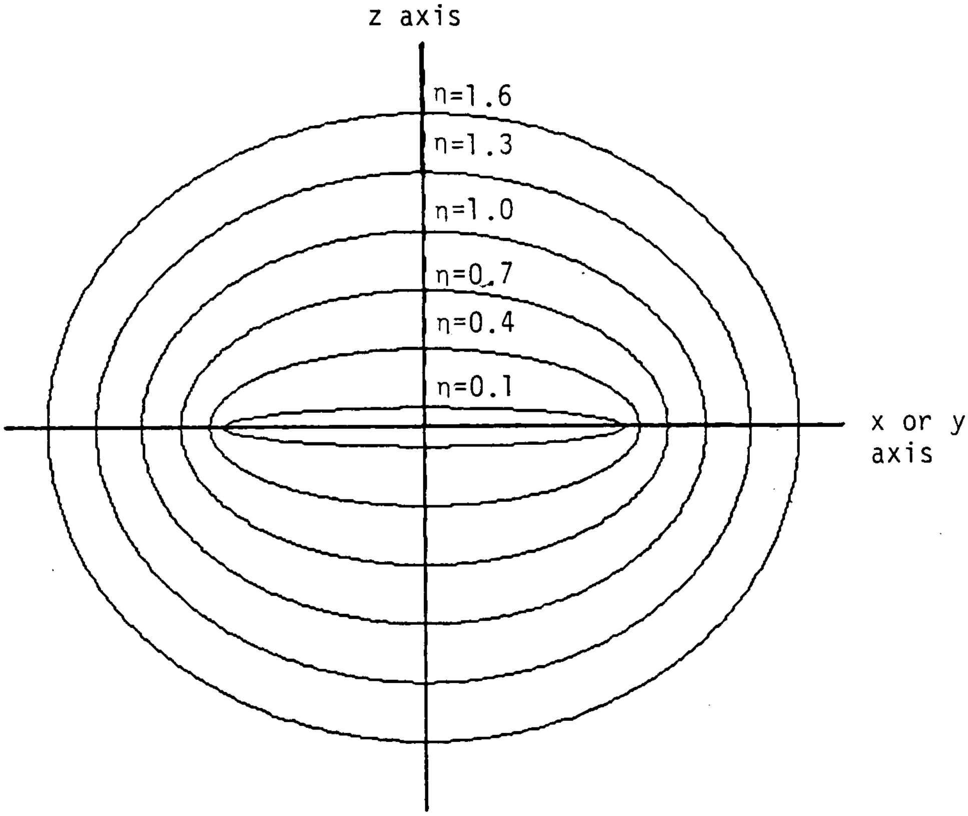

Figure 2-2. Set of ellipses with labeled shape parameters (η). Note that all the ellipses have the same focal length.

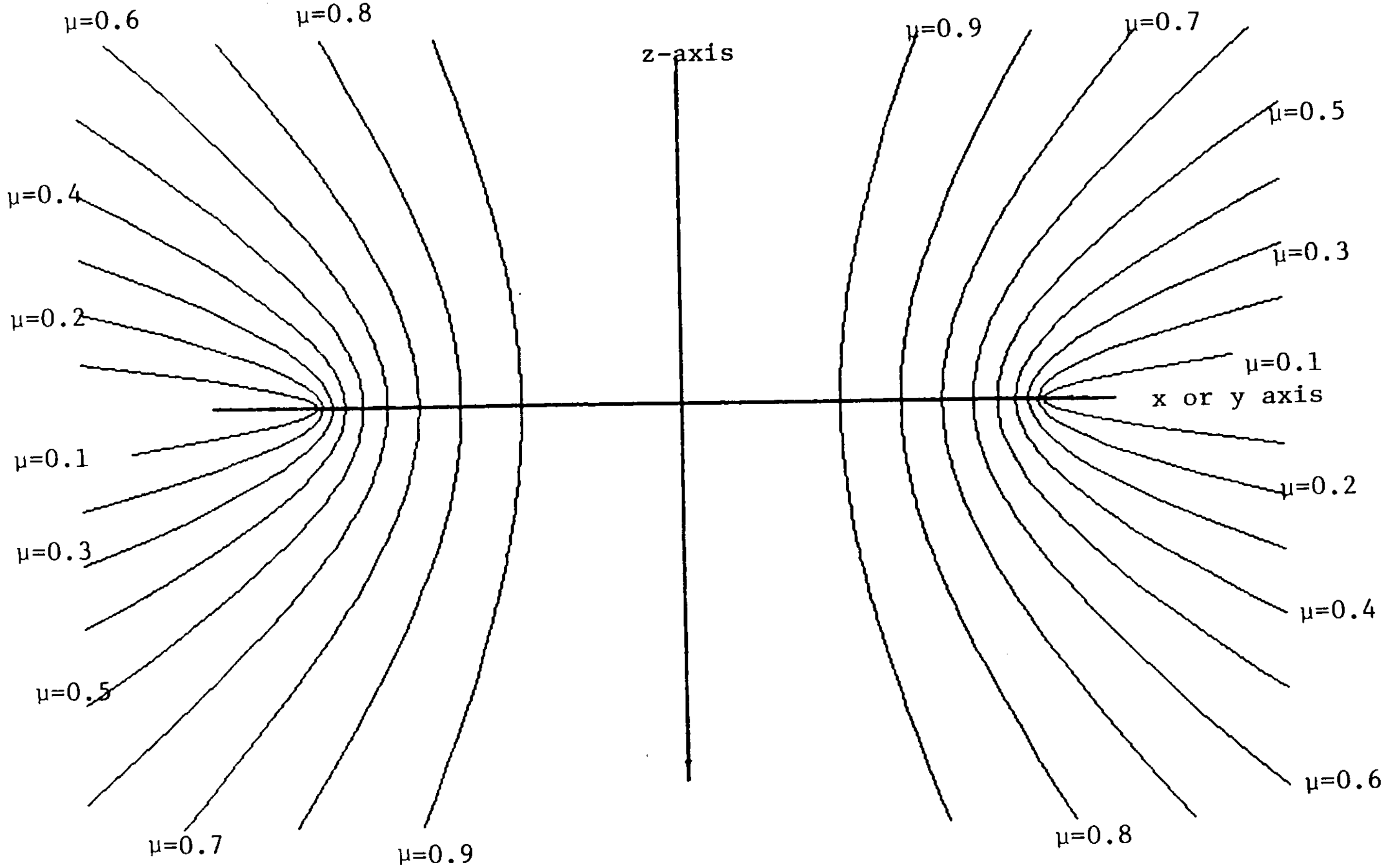

Figure 2-3. Set of hyperbolas with labeled form parameters (μ). Note that μ=0 is parallel to the x or y axis while μ=1 is parallel to the z axis.

The third set of surfaces are half planes with their edges being the z axis. The half-planes extend radially outward from the z axis. The position of a half plane is described by the angle the half plane makes with the x axis. This angle is the same as the azimuthal angle used in spherical coordinates and is denoted by ϕ where $0 \leq \phi < 2\pi$.

One can now show (see Appendix A) that any point in space (x,y,z) can also be described by coordinates (η,μ,ϕ) where

$$x = a(1 + \eta^2)^{1/2}(1 - \mu^2)^{1/2}\cos\phi \tag{2-3a}$$

$$y = a(1 + \eta^2)^{1/2}(1 - \mu^2)^{1/2}\sin\phi \tag{2-3b}$$

$$z = a\eta\mu \; . \tag{2-3c}$$

It is important in this work to note that the surface of a spheroid may be described as

$$\eta = \eta_0 = \text{constant}$$

while the inside of the spheroid is obtained for $\eta < \eta_0$ and the outside for $\eta > \eta_0$.

It should be noted here that η_0 is referred to as the shape parameter in all work below. As η_0 approaches zero, the shape of the spheroid approaches that of a disk and as η_0 approaches infinity, the spheroid assumes a spherical shape. Often it is useful to describe the shape in terms of the minor-to-major axis ratio R; this is related to the shape parameter by

$$R = \frac{\eta_0}{(1 + \eta_0^2)^{1/2}} . \tag{2-4}$$

The ratio value, R, is zero for a disk and approaches unity as the shape of the spheroid approaches that of a sphere, i.e., $0 < R < 1$.

The scale factors used in transforming differential volume elements for oblate spheroidal coordinates are given by [2.3]

$$h_\eta = a\sqrt{\frac{\eta^2 + \mu^2}{1 + \eta^2}} , \tag{2-5a}$$

$$h_\mu = a\sqrt{\frac{\eta^2 + \mu^2}{1 - \mu^2}} , \tag{2-5b}$$

$$h_\phi = a\sqrt{(1 + \eta^2)(1 - \mu^2)} . \tag{2-5c}$$

The three unit vectors $\hat{e}_\eta$, $\hat{e}_\mu$ and $\hat{e}_\phi$ are related to the Cartesian unit vectors $\hat{i}$, $\hat{j}$ and $\hat{k}$ by [2.4]

$$\hat{e}_\eta = \eta\sqrt{\frac{1 - \mu^2}{\eta^2 + \mu^2}} (\cos\phi\ \hat{i} + \sin\phi\ \hat{j}) + \mu\sqrt{\frac{1 + \eta^2}{\eta^2 + \mu^2}}\ \hat{k} \tag{2-6a}$$

$$\hat{e}_\mu = -\mu\sqrt{\frac{1 + \eta^2}{\eta^2 + \mu^2}} (\cos\phi\ \hat{i} + \sin\phi\ \hat{j}) + \eta\sqrt{\frac{1 - \mu^2}{\eta^2 + \mu^2}}\ \hat{k} \tag{2-6b}$$

$$\hat{e}_\phi = -\sin\phi\ \hat{i} + \cos\phi\ \hat{j} . \tag{2-6c}$$

B. SOLUTIONS TO LAPLACE'S EQUATION WITH BOUNDARY CONDITIONS

The forms for the potential inside and outside an oblate spheroid are shown in Appendix B to be

$$V_{in} = \sum_{\ell=0}^{\infty} \sum_{m=0}^{\ell} \sum_{p=\pm 1} A_{\ell mp} Q_{\ell m}(i\eta_0) P_{\ell m}(i\eta) Y_{\ell mp}(\beta,\phi) \tag{2-7a}$$

$$V_{out} = \sum_{\ell=0}^{\infty} \sum_{m=0}^{\ell} \sum_{p=\pm 1} B_{\ell mp} P_{\ell m}(i\eta_0) Q_{\ell m}(i\eta) Y_{\ell mp}(\beta,\phi) \ . \tag{2-7b}$$

In our samples, the spheroid size is much smaller than the wavelength of the incident light. The problem to be solved is then that of a dielectric oblate spheroid in a time varying but uniform electric field, $E_0 e^{-i\omega t}$. This is often referred to as the dipole approximation.

The $\ell=1$ terms of the Legendre functions of imaginary argument are given by [2.5]

$$P_{10}(i\eta) = i\eta \ , \tag{2-8a}$$

$$P_{11}(i\eta) = i(1 + \eta^2)^{1/2} \ , \tag{2-8b}$$

$$Q_{10}(i\eta) = \eta \ \mathrm{ctn}^{-1} \eta - 1 \ , \tag{2-8c}$$

$$Q_{11}(i\eta) = (1 + \eta^2)^{1/2}[\mathrm{ctn}^{-1} \eta - \frac{\eta}{1 + \eta^2}] \ . \tag{2-8d}$$

The $\ell=1$ terms of the real spherical harmonics are given by [2.6]

$$Y_{10}^{1}(\beta,\phi) = \sqrt{\frac{3}{4\pi}}\cos\beta \ , \tag{2-9a}$$

$$Y_{11}^{1}(\beta,\phi) = \sqrt{\frac{3}{4\pi}}\sin\beta\ \cos\phi \ , \tag{2-9b}$$

$$Y_{11}^{-1}(\beta,\phi) = \sqrt{\frac{3}{4\pi}}\sin\beta\ \cos\phi \ . \tag{2-9c}$$

The applied electric field, $\underset{\sim}{E}_0 e^{-i\omega t}$, is initially given an arbitrary direction and so the potential, at large distances away from the spheroid, due the applied electric field is

$$V = -xE_{0x}e^{-i\omega t} - yE_{0y}e^{-i\omega t} - zE_{0z}e^{-i\omega t} \ . \tag{2-10}$$

By using the relations given in Eqs. (2-3), (2-8) and (2-9), it can be shown that

$$x = -ia\sqrt{\frac{4\pi}{3}}\,P_{11}(i\eta)Y_{11}^{1}(\beta,\phi) \ , \tag{2-11a}$$

$$y = -ia\sqrt{\frac{4\pi}{3}}\,P_{11}(i\eta)Y_{11}^{-1}(\beta,\phi) \ , \tag{2-11b}$$

$$z = -ia\sqrt{\frac{4\pi}{3}}\,P_{10}(i\eta)Y_{10}^{1}(\beta,\phi) \ , \tag{2-11c}$$

so the potential at large distances can then be written as

$$V = \sum_{m=0}^{1}\sum_{p=\pm 1} ia\sqrt{\frac{4\pi}{3}}\,P_{1m}(i\eta)Y_{1mp}(\beta,\phi)E_{1mp}e^{-i\omega t} \tag{2-12}$$

where the components of the applied electric field are written as

$$E_{11}^{1} = E_{0x} \ ,$$

$$E_{11}^{-1} = E_{0y} ,$$

$$E_{10}^{1} = E_{0z} .$$

The potential as shown in Eq. (2-12) is the potential outside of the spheroid due only to the applied electric field. Any expression given for the total potential outside the spheroid must contain Eq. (2-12). The total exterior potential is then the sum of Eqs. (2-7b) and (2-12).

Because of the $e^{-i\omega t}$ time dependence of the incident field, it is convenient here to take the Fourier transform of all physical quantities. The Fourier transforms are given by [2.7]

$$\tilde{f}(\omega) = \int_{-\infty}^{+\infty} f(t)e^{i\omega t}\, dt \tag{2-13a}$$

$$f(t) = \frac{1}{2\pi} \int_{-\infty}^{+\infty} \tilde{f}(\omega)e^{-i\omega t}\, d\omega \tag{2-13b}$$

where the tilda represents the Fourier transform to frequency space. The Fourier components of the potentials inside and outside are now given by

$$V_{in} = \sum_{\ell=0}^{\infty} \sum_{m=0}^{\ell} \sum_{p=\pm 1} \tilde{A}_{\ell mp} P_{\ell m}(i\eta) Q_{\ell m}(i\eta_0) Y_{\ell mp}(\beta,\phi) , \tag{2-14a}$$

$$V_{out} = \sum_{m=0}^{1} \sum_{p=\pm 1} \sqrt{\frac{4\pi}{3}}\, ia\, P_{1m}(i\eta) Y_{1mp}(\beta,\phi) \tilde{E}_{1mp}(\omega)$$

$$+ \sum_{\ell=0}^{\infty} \sum_{m=0}^{\ell} \sum_{p=\pm 1} \tilde{B}_{\ell mp} P_{\ell m}(i\eta_0) Q_{\ell m}(i\eta) Y_{\ell mp}(\beta,\phi) . \tag{2-14b}$$

Now the two boundary conditions

$$\text{I.}\quad V_{in}\Big|_{\eta=\eta_0} = V_{out}\Big|_{\eta=\eta_0} \tag{2-15a}$$

$$\text{II.}\quad -\varepsilon(\omega)\,\frac{1}{h_\eta}\,\frac{\partial V_{in}}{\partial(i\eta)}\Big|_{\eta=\eta_0} = -\frac{1}{h_\eta}\,\frac{\partial V_{out}}{\partial(i\eta)}\Big|_{\eta=\eta_0} \tag{2-15b}$$

are applied to find the coefficients $A_{\ell mp}$ and $B_{\ell mp}$. The coefficients, with index $\ell=1$, are found to be

$$\tilde{A}_{1mp} = \frac{-ia\sqrt{\frac{4\pi}{3}}\,\tilde{E}^{(\omega)}_{1mp}W_{1m}(i\eta)}{Q_{1m}(i\eta_0)Z_{1m}(i\eta)}\Bigg|_{\eta=\eta_0} \tag{2-16a}$$

$$\tilde{B}_{1mp} = -ia\sqrt{\frac{4\pi}{3}}\,\tilde{E}^{(\omega)}_{1mp}\,[\varepsilon(\omega)-1]\,\frac{P'_{1m}(i\eta)}{Z_{1m}(i\eta)}\Bigg|_{\eta=\eta_0} \tag{2-16b}$$

where $W_{1m}(i\eta)\Big|_{\eta=\eta_0}$ is the Wronskian evaluated at the surface. The Wronskian at the surface is given by [2.8]

$$W_{1m}(i\eta)\Big|_{\eta=\eta_0} = P_{1m}(i\eta_0)Q'_{1m}(i\eta)\Big|_{\eta=\eta_0} - Q_{1m}(i\eta_0)P'_{1m}(i\eta)\Big|_{\eta=\eta_0}. \tag{2-17}$$

The term $Z_{1m}(i\eta)\Big|_{\eta=\eta_0}$ is written for convenience and is given by

$$Z_{1m}(i\eta)\Big|_{\eta=\eta_0} = \varepsilon(\omega)P'_{1m}(i\eta)\Big|_{\eta=\eta_0}Q_{1m}(i\eta_0) - P_{1m}(i\eta_0)Q'_{1m}(i\eta)\Big|_{\eta=\eta_0}. \tag{2-18}$$

The term $\varepsilon(\omega)$ is the complex dielectric response function for the spheroid.

In the dipole approximation, the terms with $\ell>1$ are not of interest, but are known to yield the resonance conditions for the quadrupole and higher order modes of oscillation. Also one finds that the coefficients $A_{\ell mp} = B_{\ell mp}$, for $\ell>1$. The $\ell=0$ terms give the potential for a charged spheroid and since the spheroid of interest here has no free charge upon it, then $A_{0mp} = B_{0mp} = 0$.

Finally, the potentials, for $\ell=1$, can be written as

$$V_{in} = \sum_{m=0}^{1} \sum_{p=\pm1} -ia \sqrt{\frac{4\pi}{3}}\, \tilde{E}_{1mp}(\omega) \left.\frac{W_{1m}(i\eta)}{Z_{1m}(i\eta)}\right|_{\eta=\eta_0} P_{1m}(i\eta)Y_{1mp}(\beta,\phi) \qquad (2\text{-}19a)$$

and

$$V_{out} = \sum_{m=0}^{1} \sum_{p=\pm1} -ia \sqrt{\frac{4\pi}{3}}\, \tilde{E}_{1mp}(\omega)\, Y_{1mp}(\beta,\phi)$$

$$\left\{\left.\frac{P'_{1m}(i\eta)}{Z_{1m}(i\eta)}\right|_{\eta=\eta_0} P_{1m}(i\eta_0)Q_{1m}(i\eta)[\varepsilon(\omega) - 1] - P_{1m}(i\eta)\right\} . \qquad (2\text{-}19b)$$

The incident field induces a surface charge density on the spheroid which may be calculated by using [2.9]

$$\sigma = \frac{1}{4\pi}\, \hat{e}_{\eta_0} \cdot \left.[\underset{\sim}{E}_{out} - \underset{\sim}{E}_{in}]\right|_{\eta=\eta_0} . \qquad (2\text{-}20)$$

Taking the negative of the gradient of the potentials given in Eqs. (2-19a) and (2-19b) to get the electric fields and using the unit vector given in Eq. (2-6a), the dipole contribution to surface charge density is found to be given by

$$\tilde{\sigma} = \sum_{m=0}^{1} \sum_{p=\pm 1} \frac{-a}{4\pi h_{\eta_0}} \sqrt{\frac{4\pi}{3}} \frac{\tilde{E}^{(\omega)}_{1mp} P'_{1m}(i\eta)\big|_{\eta=\eta_0} W_{1m}(i\eta)\big|_{\eta=\eta_0} [\varepsilon(\omega) - 1] Y_{1mp}(\beta,\phi)}{\varepsilon(\omega) P'_{1m}(i\eta)\big|_{\eta=\eta_0} Q_{1m}(i\eta_0) - P_{1m}(i\eta_0) Q'_{1m}(i\eta)\big|_{\eta=\eta_0}}$$

(2-21)

The dipole resonance condition [2.10] is given by

$$\varepsilon_{1m}(i\eta_0) = \frac{P_{1m}(i\eta_0) Q'_{1m}(i\eta)}{Q_{1m}(i\eta_0) P'_{1m}(i\eta)}\bigg|_{\eta=\eta_0} \qquad (2\text{-}22)$$

and upon using Eq. (2-22) in Eq. (2-21), the expression for the dipole surface charge density simplifies to

$$\tilde{\sigma} = \sum_{m=0}^{1} \sum_{p=\pm 1} \frac{-a}{4\pi h_{\eta_0}} \sqrt{\frac{4\pi}{3}} \frac{\tilde{E}^{(\omega)}_{1mp} W_{1m}(i\eta)\big|_{\eta=\eta_0} Y_{1mp}(\beta,\phi)[\varepsilon(\omega) - 1]}{Q_{1m}(i\eta_0)[\varepsilon(\omega) - \varepsilon_{1m}(i\eta_0)]}$$

(2-23)

The volume charge density is related to the surface charge density by [2.11]

$$\rho = \frac{\sigma\delta(\eta - \eta_0)}{h_{\eta_0}} \, . \qquad (2\text{-}24)$$

The dipole volume charge density is then

$$\tilde{\rho} = \frac{-\delta(\eta - \eta_0)}{4\pi a^2(\eta_0^2 + a^2)} \sqrt{\frac{4\pi}{3}} \sum_{m=0}^{1} \sum_{p=\pm 1} \frac{(-1)^m (1+m)! \tilde{E}^{(\omega)}_{1mp} Y_{1mp}(\beta,\phi)[\varepsilon(\omega) - 1]}{Q_{1m}(i\eta_0)[\varepsilon(\omega) - \varepsilon_{1m}(i\eta_0)]}$$

(2-25)

where the expression for the Wronskian [2.12] has been used.

With this expression for the dipole volume charge density, the three components of the induced dipole moment can be found by using [2.13]

$$\tilde{p}_x = \tilde{p}^1_{11} = \int h_\eta d\eta \int h_\mu d\mu \int h_\phi d\phi \, \tilde{\rho} \, x \tag{2-26}$$

and also similar expression for the y and z components. Upon substituting in the relations given in Eqs. (2-5a) through (2-5c), (2-11a) through (2-11c) and (2-25) into Eq. (2-26), the three components of the dipole moments are found to be

$$\tilde{p}_x = \tilde{p}^1_{11} = \frac{2a^3(1+\eta_0^2)^{1/2}[\varepsilon(\omega)-1]}{3Q_{11}(i\eta_0)[\varepsilon(\omega)-\varepsilon_{11}(i\eta_0)]} \tilde{E}_x(\omega) = \alpha_x \tilde{E}_x(\omega) \ , \tag{2-27a}$$

$$\tilde{p}_y = \tilde{p}^{-1}_{11} = \frac{2a^3(1+\eta_0^2)^{1/2}[\varepsilon(\omega)-1]}{3Q_{11}(i\eta_0)[\varepsilon(\omega)-\varepsilon_{11}(i\eta_0)]} \tilde{E}_y(\omega) = \alpha_y \tilde{E}_y(\omega) \ , \tag{2-27b}$$

$$\tilde{p}_z = p^1_{10} = \frac{-a^3\eta_0[\varepsilon(\omega)-1]}{3Q_{10}(i\eta_0)[\varepsilon(\omega)-\varepsilon_{10}(i\eta_0)]} \tilde{E}_z(\omega) = \alpha_z \tilde{E}_z(\omega) \ . \tag{2-27c}$$

The terms α_x, α_y and α_z are the polarizabilities of the spheroid along the three axes. The polarizability tensor is thus diagonal with two of the elements on the diagonal being equal ($\alpha_x = \alpha_y$).

From these expressions for the induced dipole moments, the scattered fields at large distances from the spheroid can be calculated [2.14]

$$\underset{\sim}{E}_{sca} = \frac{\omega^2 e^{i\underset{\sim}{k}\cdot\underset{\sim}{r}}}{c^2 r} [(\hat{n} \times \underset{\sim}{p}) \times \hat{n}] \tag{2-28}$$

where $\hat{n}$ is a unit vector in the direction of observation and $\underset{\sim}{p}$ is the induced dipole moment.

C. DIPOLE SCATTERING AND ABSORPTION CROSS SECTIONS

The total cross section is derived using the optical theorem [2.15]. It is the sum of the scattering and absorption cross sections.

Consider an oblate spheroid with a plane monochromatic electromagnetic wave incident upon it. If the spheroid is made of metal, then part of the incident energy contained in the electromagnetic wave is absorbed and the rest is reradiated by scattering. The Poynting vector [2.16] gives the flux of energy per unit area per unit time. The time-averaged Poynting vector outside the spheroid is given by

$$\langle \underset{\sim}{S} \rangle = \frac{c}{8\pi} \mathrm{Re}[\underset{\sim}{E} \times \underset{\sim}{H}^*] \ . \tag{2-29}$$

Were it not for absorption, $\langle \underset{\sim}{S} \rangle$ would be zero when integrated over a large sphere surrounding the spheroid, for then just as much energy leaves as enters the sphere each second.

The electric field outside the spheroid is the sum of the incident electric field and the scattered electric field. Similarly, the magnetic field outside is the sum of the incident and scattered magnetic fields. This can be expressed as

$$\underset{\sim}{E} = \underset{\sim}{E}_0 + \underset{\sim}{E}_{sca} \tag{2-30a}$$

and

$$\underset{\sim}{H} = \underset{\sim}{H}_0 + \underset{\sim}{H}_{sca} \ . \tag{2-30b}$$

The time-averaged Poynting vector represents the power per unit area. If Eq. (2-29) is integrated over the surface of a large sphere that encloses the spheroid, then the result is the net flow of energy per second either into or out of the sphere. Since the spheroid within the sphere is a metal and will absorb energy, the power absorbed within the sphere obtained from using Eqs. (2-29), (2-30a) and (2-30b) is

$$P_{abs} = -\frac{c}{8\pi}\int \mathrm{Re}[\underset{\sim}{E}_0 \times \underset{\sim}{H}_0^* + \underset{\sim}{E}_{sca} \times \underset{\sim}{H}_0^* + \underset{\sim}{E}_0 \times \underset{\sim}{H}_{sca}^* + \underset{\sim}{E}_{sca} \times \underset{\sim}{H}_{sca}^*] \cdot \hat{n}\, da \ . \tag{2-31}$$

The scattered power, P_{scat}, is the energy per second leaving the sphere; viz.,

$$P_{scat} = \frac{c}{8\pi}\int \mathrm{Re}[\underset{\sim}{E}_{sca} \times \underset{\sim}{H}_{sca}^*] \cdot \hat{n}\, da \ . \tag{2-32}$$

The sum of Eqs. (2-31) and (2-32) gives the total time-averaged power, P_{total}, being dissipated by the spheroid from both scattering and absorption.

$$P_{total} = -\frac{c}{8\pi}\int \mathrm{Re}[\underset{\sim}{E}_0 \times \underset{\sim}{H}_0^* + \underset{\sim}{E}_0 \times \underset{\sim}{H}_{sca}^* + \underset{\sim}{E}_{sca} \times \underset{\sim}{H}_0^*] \cdot \hat{n}\, da \ . \tag{2-33}$$

The first cross product of Eq. (2-33) is proportional to the time-averaged Poynting vector of the incident electromagnetic wave. This can be shown to be zero upon integrating over the sphere and so the total power dissipated by both scattering and absorption is

$$P_{total} = -\frac{c}{8\pi}\int \mathrm{Re}[\underset{\sim}{E}_0 \times \underset{\sim}{H}^*_{sca} + \underset{\sim}{E}_{sca} \times \underset{\sim}{H}^*_0]\cdot\hat{n}\, da \ . \tag{2-34}$$

The total cross section is the ratio of the total power dissipated by absorption and scattering to the incident power per unit area [2.17]. The total cross section is then

$$\sigma_{total} = \frac{-\frac{c}{8\pi}\int \mathrm{Re}[\underset{\sim}{E}_0 \times \underset{\sim}{H}^*_{sca} + \underset{\sim}{E}_{sca} \times \underset{\sim}{H}^*_0]\cdot\hat{n}\, da}{\frac{c}{8\pi}\,\mathrm{Re}|E_0|^2} \ . \tag{2-35}$$

From Maxwell's equations, it can be shown that the electric and magnetic fields of a transverse electromagnetic wave in a vacuum are related by [2.18]

$$\underset{\sim}{E} = \hat{n} \times \underset{\sim}{H} \tag{2-36a}$$

and

$$\underset{\sim}{H} = \hat{n} \times \underset{\sim}{E} \ . \tag{2-36b}$$

The total cross section can now be written

$$\sigma_{total} = \frac{-\int \mathrm{Re}[\underset{\sim}{E}_0 \times (\hat{n} \times \underset{\sim}{E}^*_{sca}) + \underset{\sim}{E}_{sca} \times (\hat{n}_0 \times \underset{\sim}{E}^*_0)]\cdot\hat{n}\, da}{\mathrm{Re}|E_0|^2} \ . \tag{2-37}$$

The element of surface area da, in spherical coordinates, is given by

$$da = r^2 \sin\theta \, d\theta \, d\phi \; . \tag{2-38}$$

The unit vector $\hat{n}$ is in the direction of observation and is related to the cartesian unit vectors $\hat{i}$, $\hat{j}$, and $\hat{k}$ by

$$\hat{n} = \sin\theta\cos\phi\hat{i} + \sin\theta\sin\phi\hat{j} - \cos\theta\hat{k} \; . \tag{2-39}$$

The unit vector $\hat{n}_0$ is in the direction of propagation of the incident wave and is related to the cartesian unit vectors by

$$\hat{n}_0 = \sin\Theta\,\hat{j} - \cos\Theta\,\hat{k} \; . \tag{2-40}$$

The scattered fields are related to the incident fields (see Eq. (2-28)) by the dipole moments in Eqs. (2-27a) through (2-27c). The incident electric fields for both polarizations (s and p) are given by

$$\underset{\sim}{E}_s = \underset{\sim}{E}_0 \, e^{i(\underset{\sim}{k}\cdot\underset{\sim}{r})}\hat{i} \tag{2-41a}$$

$$\underset{\sim}{E}_p = \underset{\sim}{E}_0 \, e^{i(\underset{\sim}{k}\cdot\underset{\sim}{r})}(\cos\Theta\,\hat{j} + \sin\Theta\,\hat{k}) \; . \tag{2-41b}$$

Upon substituting the proper incident and scattered electric fields and the equations given for the unit vectors $\hat{n}$ and $\hat{n}_0$, the cross sections for both polarizations (s and p) are found to be

$$\sigma_{total}\Big|_{s\text{-}pol} = \frac{4\pi\omega}{c}\,\mathrm{Im}\,\{\alpha_x\} \tag{2-42a}$$

$$\sigma_{total}\Big|_{p\text{-}pol} = \frac{4\pi\omega}{c}\,\mathrm{Im}\,\{\alpha_y\cos^2\Theta + \alpha_z\sin^2\Theta\} \; . \tag{2-42b}$$

The details of the integrations are rather long and tedious and are included in Appendix C.

It is useful to distinguish between the incident light that is absorbed and that which is scattered. The scattering cross section is defined as the ratio of the scattered power to the incident power per unit area [2.19]

$$\sigma_{sca} = \frac{\frac{c}{8\pi}\int \mathrm{Re}[\underset{\sim}{E}_{sca} \times \underset{\sim}{H}^*_{sca}] \cdot \hat{n}\, da}{\frac{c}{8\pi}\,\mathrm{Re}|E_0|^2} . \tag{2-43}$$

Substituting in the form of the scattered magnetic field given in Eq. (2-36b) and simplifying the triple vector product gives

$$\sigma_{sca} = \frac{\int \mathrm{Re}[\hat{n}|\underset{\sim}{E}_{sca}|^2] \cdot \hat{n}\, da}{\mathrm{Re}|E_0|^2} . \tag{2-44}$$

Using the relation for the scattered electric field given in Eq. (2-28), the scattering cross section is seen to be

$$\sigma_{sca} = \frac{\int \mathrm{Re}[\frac{\omega^4}{c^4 r^2} (\underset{\sim}{p} - \hat{n}(\underset{\sim}{p} \cdot \hat{n})) \cdot (\underset{\sim}{p}^* - \hat{n}(\underset{\sim}{p}^* \cdot \hat{n}))] \cdot \hat{n}\, da}{\mathrm{Re}|E_0|^2} . \tag{2-45}$$

The scattering cross sections take on different forms for each polarization of the incident field. Thus,

$$\sigma_{sca}\Big|_{s\text{-pol}} = \frac{\omega^4}{c^4}\int |\alpha_x|^2 \{1 - \sin^2\theta\cos^2\phi\} da \tag{2-46a}$$

and

$$\sigma_{sca}\Big|_{s\text{-pol}} = \frac{\omega^4}{c^4}\int \{|\alpha_y|^2 \cos^2 \Theta + |\alpha_z|^2 \sin^2 \Theta$$

$$- |\alpha_y|^2 \cos^2 \Theta \sin^2\theta \sin^2\phi - |\alpha_z|^2 \sin^2 \Theta \cos^2\theta$$

$$- (\alpha_y^*\alpha_z + \alpha_y\alpha_z^*) \sin \Theta \cos \Theta \sin\theta\cos\theta\sin\phi\}da \ , \tag{2-46b}$$

Upon integrating Eqs. (2-46a) and (2-46b), the scattering cross sections become

$$\sigma_{sca}\Big|_{s\text{-pol}} = \frac{8\pi\omega^4}{3c^4} |\alpha_x|^2 \tag{2-47a}$$

and

$$\sigma_{sca}\Big|_{p\text{-pol}} = \frac{8\pi\omega^4}{3c^4} \{|\alpha_y|^2 \cos^2 \Theta + |\alpha_z|^2 \sin^2 \Theta\} \ . \tag{2-47b}$$

The cross sections for pure absorption are obtained by subtracting Eq. (2-47a) from (2-42a) for s-polarization and Eq. (2-47b) from (2-42b) for p-polarization.

It is obvious that, for the case where the spheroid is composed of a lossless dielectric material, the total cross sections of Eqs. (2-42a) and (2-42b) are zero. For this case, the total cross sections are just the scattering cross sections of Eqs. (2-47a) and (2-47b).

D. ANALYSIS OF THE CROSS SECTIONS

The total cross sections were given in Eqs. (2-42a) and (2-42b). Most of the information concerning the heights and positions of the peaks in the cross sections are contained in the expressions for the polarizabilities. These were given in Eqs. (2-27a), (2-27b) and (2-27c) and for convenience are given again here as

$$\alpha_x = \alpha_y = \frac{2a^3(1 + \eta_0^2)^{1/2}[\varepsilon(\omega) - 1]}{3Q_{11}(i\eta_0)[\varepsilon(\omega) - \varepsilon_{11}(i\eta_0)]} \tag{2-48a}$$

$$\alpha_z = \frac{-a^3\eta_0[\varepsilon(\omega) - 1]}{3Q_{10}(i\eta_0)[\varepsilon(\omega) - \varepsilon_{10}(i\eta_0)]} \; . \tag{2-48b}$$

Peaks in the cross sections occur when the denominators of the polarizability expressions are a minimum. The peaks are then located at the wavelength for which Re $\varepsilon(\omega) = \varepsilon_{1m}(i\eta_0)$. The peaks are kept finite by the imaginary part of the dielectric response function, $\varepsilon(\omega)$. The real and imaginary parts of the dielectric response function are obtained from the experimental bulk optical data [2.20] for the material of interest.

It is now useful to examine the form of the resonance condition, which is termed the shape dependent dielectric function. There are two resonance conditions for the dipole mode (ℓ=1) corresponding to the two allowed values of the index m (m=0 or m=1). The m=0 mode corresponds to a dipole resonance along the minor (z) axis while the m=1 mode corresponds to a resonance along the major (x or y) axis. A plot of the shape dependent dielectric function, $\varepsilon_{1m}(i\eta_0)$, versus the shape parameter is shown in Figure 2-4. The same curves, plotted as a function of the minor-to-major axis ratio, are shown in

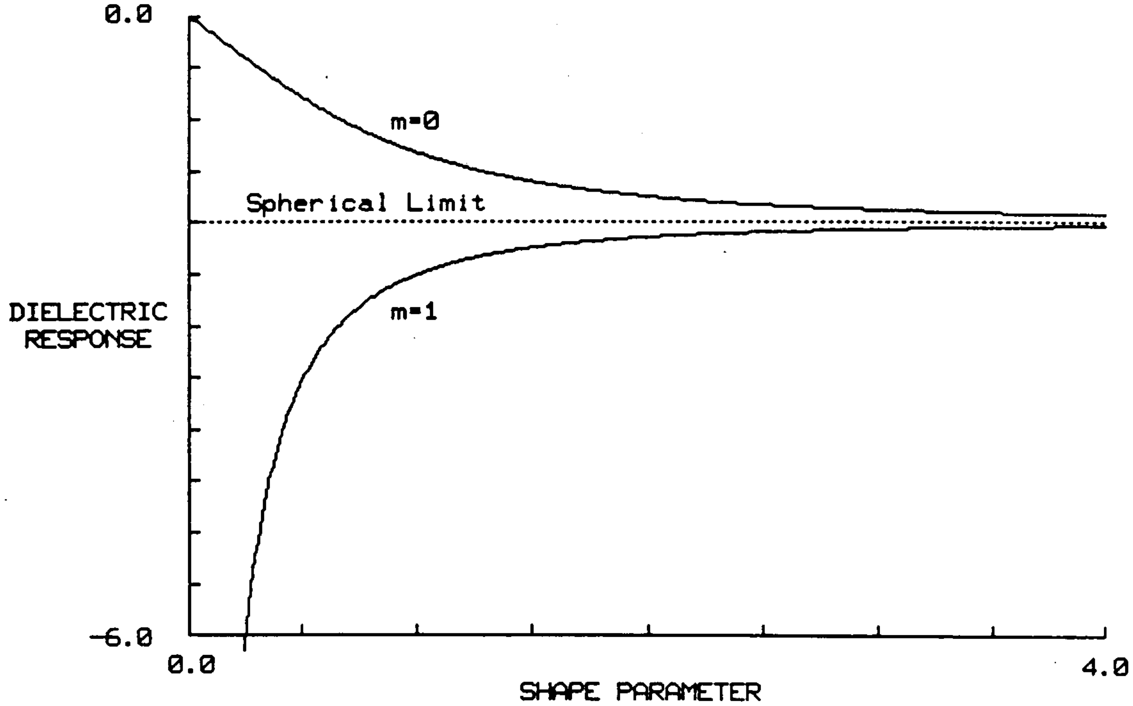

Figure 2-4. The shape dependent dielectric response function, $\epsilon_{1m}(i\eta)$, versus the shape parameter η. Note that both the m=0 and m=1 modes converge to the same value as the shape approaches that of a sphere.

Figure 2-5. The two curves in each plot correspond to the two different modes. One can see that under certain conditions there may be two peaks in the cross section owing to the two different dipole modes. Figure 2-6 is a plot of the shape parameter versus the wavelength at which the value of the shape dependent dielectric function, $\varepsilon_{1m}(i\eta_0)$, is equal to the real part of the experimental bulk dielectric response function, $\varepsilon(\omega)$, for silver. Figure 2-7 is the same plot except the minor-to-major axis ratio occupies the axis of ordinates.

There are two factors determining the heights of the peaks. The first is the wavelength. Note the factor of ω/c in the absorption cross section. The absorption is thus inversely proportional to the wavelength. The scattering cross section contains a factor ω^4/c^4 and so is inversely proportional to fourth power of the wavelength. The second factor affecting the height is the volume of the spheroid. Note the factors of $a^3(1 + \eta_0^2)^{1/2}$ or $a^3\eta_0$ in the expressions for the polarizabilities given in Eqs. (2-48a) and (2-48b).

The volume of an oblate spheroid is given by [2.21]

$$V = \frac{4\pi}{3} r_0^2 z_0 \tag{2-49}$$

where r_0 is the semimajor axis length and z_0 is the semiminor axis length. The semimajor axis length is related to the focal length and shape parameter by

$$r_0 = a(1 + \eta_0^2)^{1/2} \tag{2-50}$$

while the semiminor axis length is related by

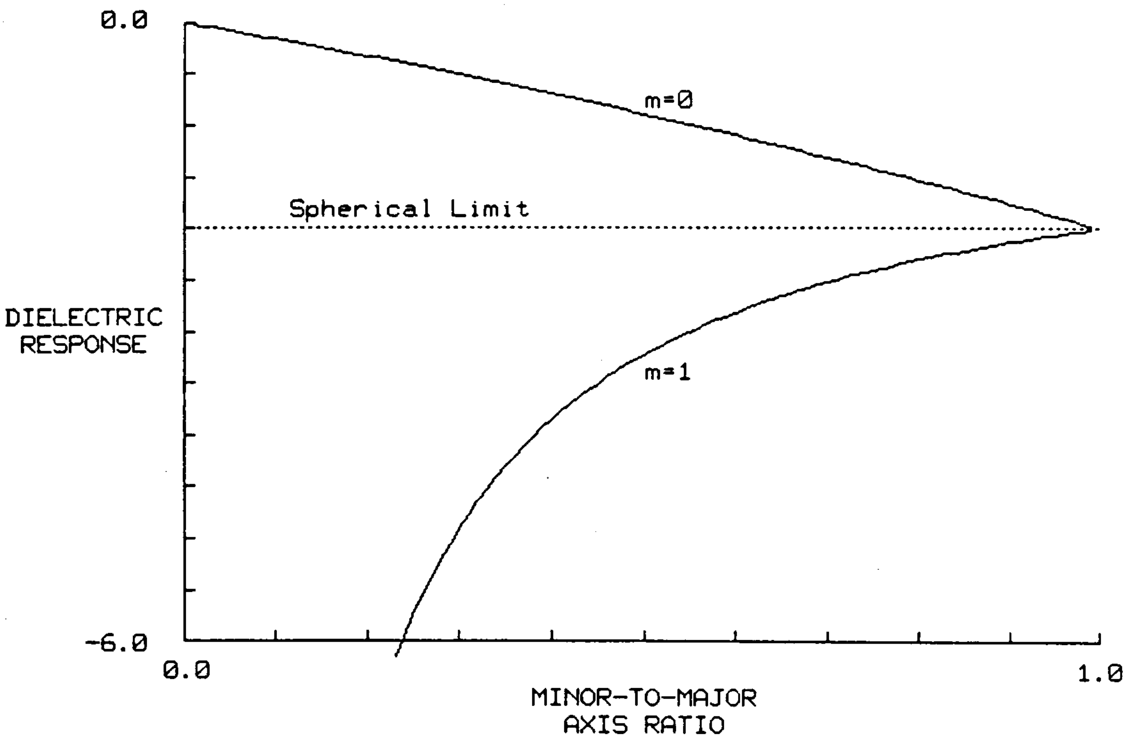

Figure 2-5. The shape dependent dielectric response function, $\varepsilon_{1m}(i\eta)$, versus the minor-to-major axis ratio, R.

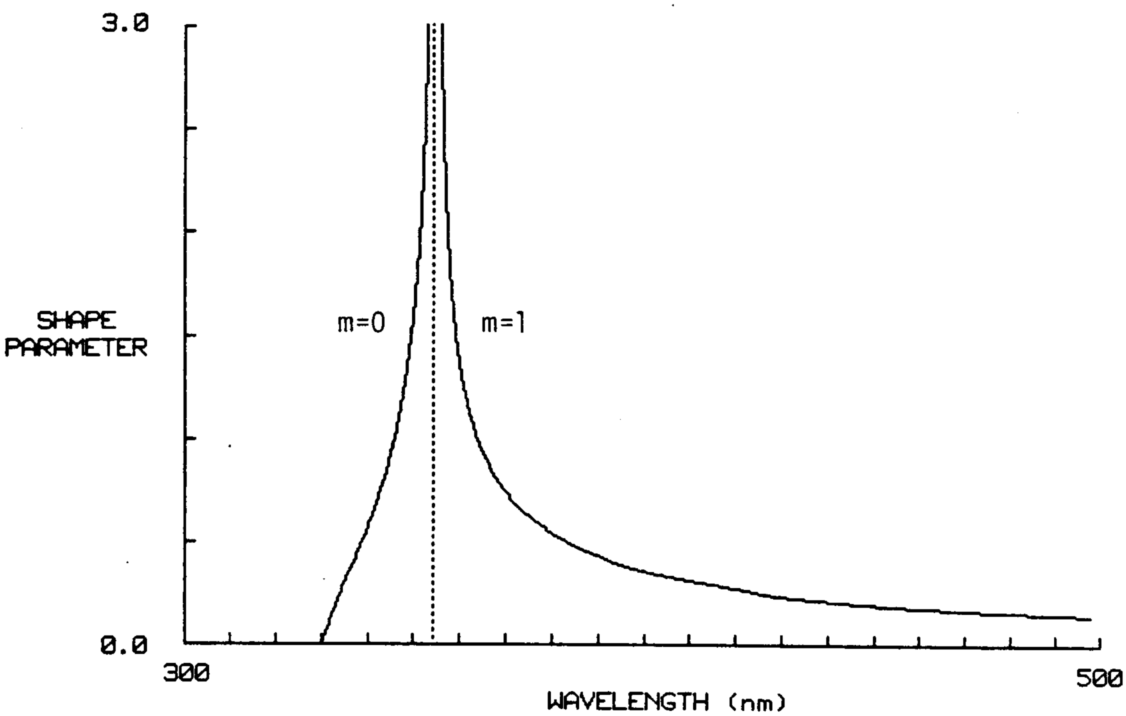

Figure 2-6. Shape parameter versus wavelength. This is for silver oblate spheroids and is the shape and wavelength for which $\varepsilon_{1m}(i\eta)$ equals $\mathrm{Re}\,\varepsilon(\omega)$ from the experimental optical data.

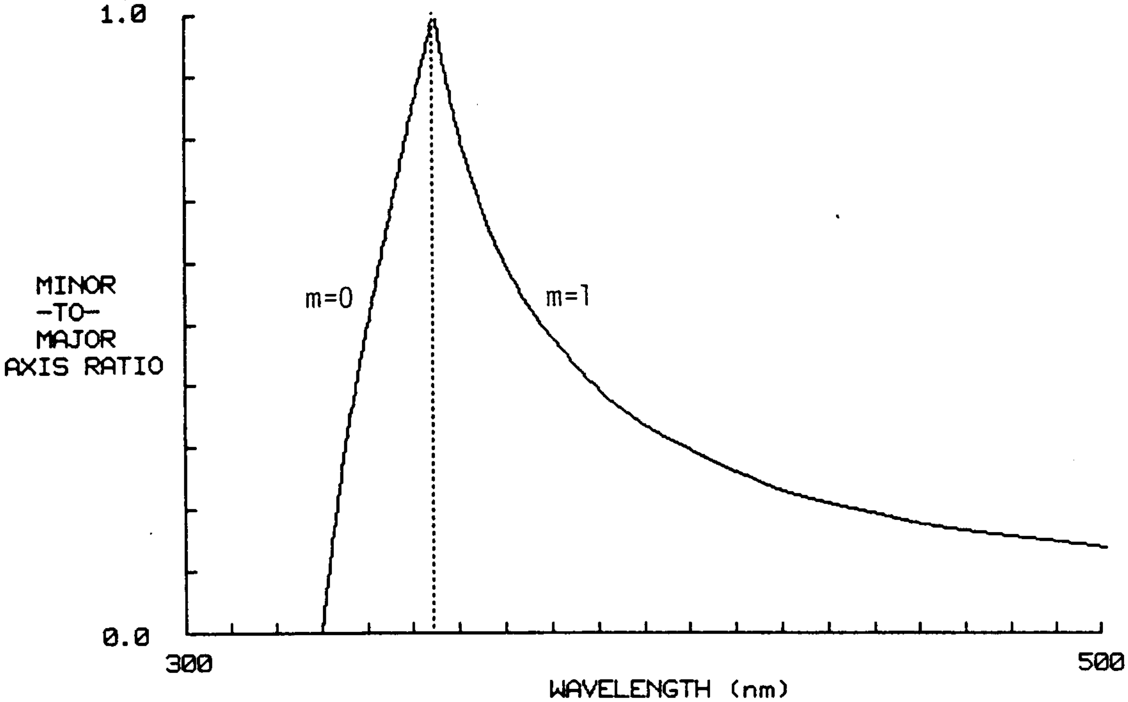

Figure 2-7. Minor-to-major axis ratio versus wavelength. This is for silver oblate spheroids and is the minor-to-major axis ratio and wavelength for which $\varepsilon_{1m}(i\eta)$ equals Re $\varepsilon(\omega)$ from the experimental optical data.

$$z_0 = a\eta_0 \ . \tag{2-51}$$

The volume of the spheroid in terms of the focal length and shape parameter is then

$$V = \frac{4\pi}{3} a^3(1 + \eta_0^2)\eta_0 \ . \tag{2-52}$$

Upon referring back to Eqs. (2-48a) and (2-48b), one can see that the polarizabilities are proportional to the volume of the spheroid.

The scattering cross section is thus proportioal to $V^2\lambda^{-4}$, while absorption is proportional to $V\lambda^{-1}$ [2.22]. Upon combining Eqs. (2-4), (2-50) and (2.52) one can see that the volume of the spheroid may be expressed in terms of the semimajor axis length and the minor-to-major axis ratio as

$$V = \frac{4\pi}{3} r_0^3 R \ . \tag{2-53}$$

Note that a minor-to-major axis ratio value of unity corresponds to a sphere and that this expression reduces to the usual expression for the volume of a sphere for R=1. In Figures 2-8 and 2-9, the scattering and absorption cross sections versus wavelength have been plotted. The cross sections were calculated for normally incident light of either polarization. The various curves represent the cross sections with several different minor-to-major axis ratios. All were calculated using the same semimajor axis length. By holding the semimajor axis length constant and increasing the minor-to-major axis ratio, one can see by Eq. (2-53) that the volume of the spheroid becomes larger.

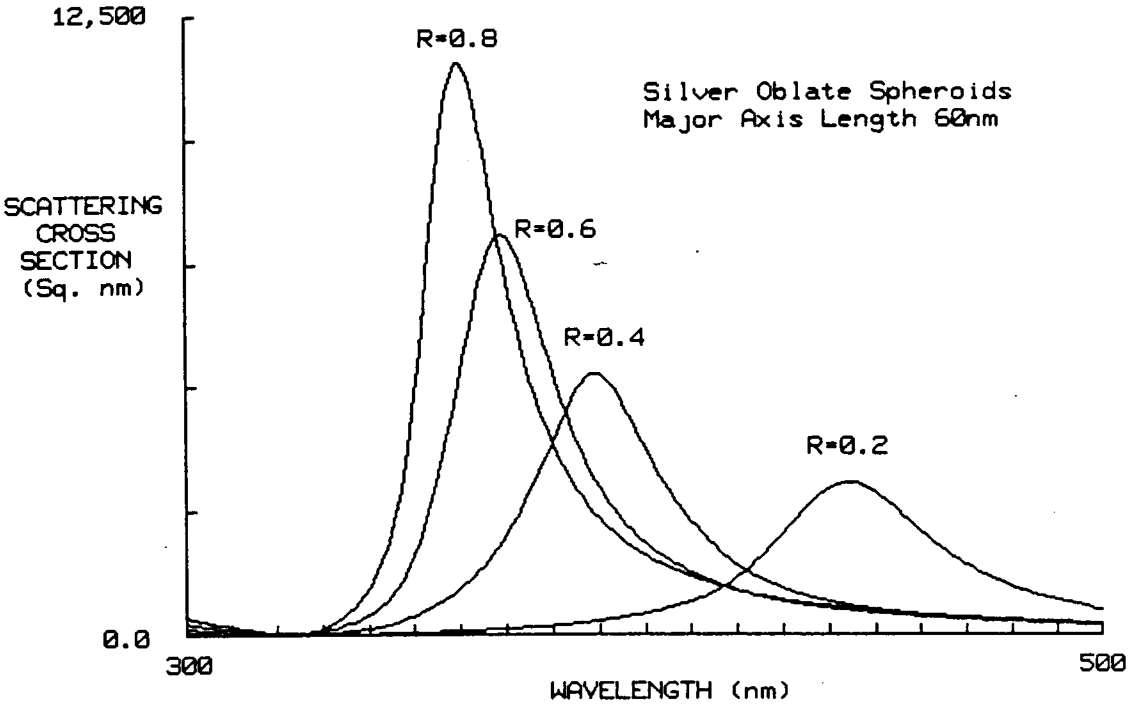

Figure 2-8. Scattering cross section versus wavelength. The cross sections were calculated using minor-to-major axis ratios of 0.2, 0.4, 0.6, and 0.8 but all with the same semi-major axis length of 30 nm. All curves are for normal incidence.

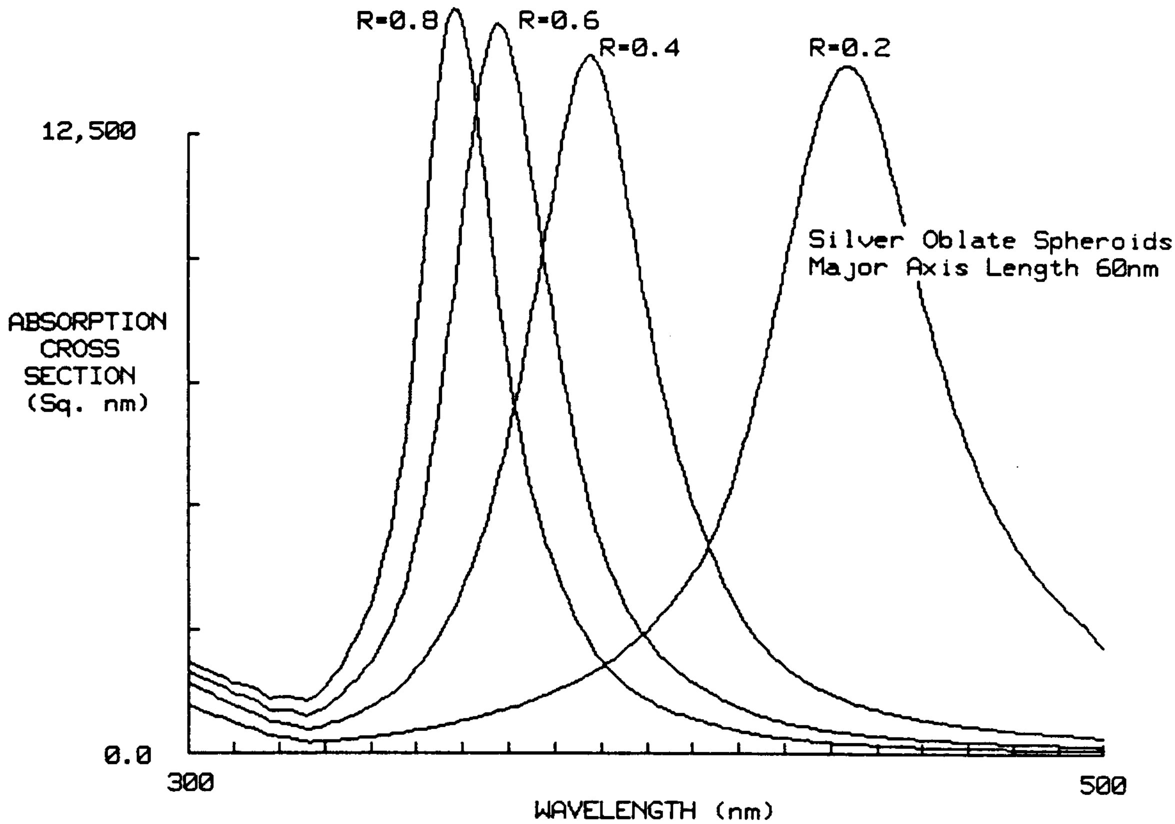

Figure 2-9. Absorption cross section versus wavelength. The cross sections were calculated using minor-to-major axis ratios of 0.2, 0.4, 0.6, and 0.8 but all with the same semi-major axis length of 30 nm.

From the maximums in the cross sections, one can see that scattering will dominate for particles with larger volumes and at shorter wavelengths. The absorption cross section is affected less by changes in volume and wavelength and so the maximum in its cross section changes relatively little in magnitude for various shapes of particles.

E. SPHERICAL LIMITS

In the limit where the shape parameter, η_0, approaches infinity, the ellipsoids become spheres. In this limit, the polarizabilities shown in Eqs. (2-48a) and (2-48b) should equal the well known form of the polarizability of a sphere [2.23].

$$\alpha_{sphere} = r^3 \frac{[\varepsilon(\omega) - 1]}{[\varepsilon(\omega) + 2]}$$

where r is the radius of the sphere.

The z component of the polarizability is given by Eq. (2-48b)

$$\alpha_z = \frac{-a^3\eta_0[\varepsilon(\omega) - 1]}{3Q_{10}(i\eta_0)[\varepsilon(\omega) - \varepsilon_{10}(i\eta_0)]} \ .$$

From Figure 2-4, it is seen that $\varepsilon_{1m}(i\eta_0)$ approaches the value of -2 as η_0 approaches infinity so the terms containing the dielectric functions are easily shown to converge properly

$$\lim_{\eta_0 \to \infty} \frac{[\varepsilon(\omega) - 1]}{[\varepsilon(\omega) - \varepsilon_{10}(i\eta_0)]} = \frac{[\varepsilon(\omega) - 1]}{[\varepsilon(\omega) + 2]}$$

The remaining terms of Eq. (2-48b) must then converge to r^3.

The semiminor axis should equal the radius as η_0 approaches infinity. Using the expression for $Q_{10}(i\eta_0)$ given in Eq. (2-8c) and for the semiminor axis using Eq. (2-51), the remaining terms become

$$\lim_{\eta_0 \to \infty} \frac{-a^3 \eta_0}{3Q_{10}(i\eta_0)} = \lim_{\eta_0 \to \infty} \frac{-Z_0^3}{3\eta_0^2[\eta_0 \operatorname{ctn}^{-1}\eta_0 - 1]} . \tag{2-54}$$

The series expansion for the inverse cotangent (for $\eta_0 > 1$) is given by [2.24]

$$\operatorname{ctn}^{-1}\eta_0 = \frac{1}{\eta_0} - \frac{1}{3\eta_0^3} + \frac{1}{5\eta_0^5} - \frac{1}{7\eta_0^7} + \ldots$$

Now upon substituting in the series expansion into Eq. (2-54), one can see that all but the first two terms will go to zero as η_0 approaches infinity and so keeping only the first two terms

$$\lim_{\eta_0 \to \infty} \frac{-Z_0^3}{3\eta_0^2[1 - \frac{1}{3\eta_0^2} - 1]} = Z_0^3 \tag{2-55}$$

and so the polarizability along the minor axis becomes

$$\lim_{\eta_0 \to \infty} \alpha_z = Z_0^3 \frac{[\varepsilon(\omega) - 1]}{[\varepsilon(\omega) - \varepsilon_{10}(i\eta_0)]} . \tag{2-56}$$

The polarizability along the major axis is given by Eq. (2-48a)

$$\alpha_x = \alpha_y = \frac{2a^3(1 + \eta_0^2)^{1/2}[\varepsilon(\omega) - 1]}{3Q_{11}(i\eta_0)[\varepsilon(\omega) - \varepsilon_{11}(i\eta_0)]} .$$

Again from Figure 2-4, the terms containing the dielectric functions are seen to converge properly

$$\lim_{\eta_0 \to \infty} \frac{[\varepsilon(\omega) - 1]}{[\varepsilon(\omega) - \varepsilon_{11}(i\eta_0)]} = \frac{[\varepsilon(\omega) - 1]}{[\varepsilon(\omega) + 2]} .$$

For this case, the semimajor axis should equal the radius as η_0 approaches infinity. Using the expression for $Q_{11}(i\eta_0)$ given in Eq. (2-8d) and expressing the semimajor axis as in Eq. (2-50), then the remaining terms in Eq. (2-48a) are

$$\lim_{\eta_0 \to \infty} \frac{2a^3(1 + \eta_0^2)^{1/2}}{3Q_{11}(i\eta_0)} = \lim_{\eta_0 \to \infty} \frac{2r_0^3}{3(1 + \eta_0^2)^{3/2}[\mathrm{ctn}^{-1}\eta_0 - \frac{\eta_0}{1 + \eta_0^2}]} . \quad (2\text{-}57)$$

Again, all but the first two terms of the series expansion for inverse cotangent will converge to zero as η_0 approaches infinity. Upon substituting in the first two terms of the expansion and after some manipulation, Eq. (2-57) becomes

$$\lim_{\eta_0 \to \infty} \frac{2r_0^3}{[3(1 + \frac{1}{\eta_0^2})^{1/2} - (1 + \frac{1}{\eta_0^2})^{3/2}]} .$$

The terms in the denominator may be expanded using the binomial expansion for $(1+X)^{n/2}$ [2.25]. Upon keeping only the first two terms of these expansions

$$\lim_{\eta_0 \to \infty} \frac{2r_0^3}{[3(1 + \frac{1}{2\eta_0^2}) - (1 + \frac{3}{2\eta_0^2})]} = r_0^3 \ .$$

The expression for the polarizability along the major axis in Eq. (2-48a) is now seen to be

$$\lim_{\eta_0 \to \infty} \alpha_x = \lim_{\eta_0 \to \infty} \alpha_y = r_0^3 \frac{[\varepsilon(\omega) - 1]}{[\varepsilon(\omega) + 2]} \ .$$

CHAPTER III

EXPERIMENT

In this thesis, the experimental work consists of measuring the optical absorbance of silver particles on quartz substrates as a function of wavelength, polarization and angle of incidence.

In the first section of this chapter, a description of the sample preparation and characterization technique is given. In the following section, the instrumentation is described. To enable a rapid and quantitative analysis of the data, the data were digitized and stored in computer memory. This procedure is discussed in the last section.

A. SAMPLE PREPARATION AND CHARACTERIZATION

In the work presented here, silver films were evaporated onto quartz slides at a pressure of approximately 5.0×10^{-6} torr. All film thicknesses were 5 nm (±0.5 nm) as measured by a quartz crystal thickness monitor. In order to minimize the coalescence growth [3.1] of the films, rather high rates of evaporation (≈1 nm/sec) were used. The quartz slides, which measured ≈1.7 cm x 6.0 cm x 0.16 cm, were cut from a polished quartz plate [3.2]. The quartz slides were cleaned first by hand with a mixture of MICRO [3.3] and distilled water. The slides were then rinsed thoroughly with distilled water, with isopropyl alcohol and finally with distilled water again.

Immediately after the final rinsing, the slide was blown dry and placed in the vacuum evaporator.

After the evaporation of 5 nm of silver onto the surface, the slide was placed into a resistively heated oven [3.4] for roughly 30 seconds. This time can be varied a few seconds with negligible effect. The oven temperature, as measured with a chromel-alumel thermocouple, was about 750°C. During heating, the film changed from a violet to yellow color as viewed by transmission. The heat treatment time was chosen such that it would yield a uniform sample color. A shorter stay in the oven (around 10 seconds) produced the yellow color around the perimeter of the slide while the center area was still violet. This indicated different particle characteristics in the different regions. If the slide was placed in the oven shortly afterward, a larger portion of the slide appeared yellow as viewed by transmission. To obtain uniformity in color and particle characteristics, all subsequent slides were placed in the oven for about 30 seconds. This was sufficient to produce the requisite uniformity in color.

There was some concern about the formation of a contaminating layer on the surface of the silver, especially during the heating process. Silver is subject to the formation of silver sulfide on its surface. Because of this concern, a slow but steady stream of argon was allowed to flow through the oven while the sample was being heated. Also, all data were taken on the sample within two hours of evaporation. It is believed that these two factors were sufficient to minimize any effect a contaminating layer on the surface may have had on the optical measurements.

After the optical data were taken, the sample was overcoated with a conducting layer (approximately 30 nm) of evaporated silver. (The sample surface can only be viewed with the aid of a scanning electron microscope (SEM) [3.5] if its entire surface is conducting.) The conducting layer was also evaporated at a rate of 1 nm/sec. This high rate was thought to reduce the coalescence growth of the added film and thus reduce the distortion of surface geometries.

When viewed with the SEM, the sample displayed many particles with some variety in size. Nearly all of the particles appeared to have circular cross sections as viewed at normal incidence. Views of the surface profile from nonnormal incidence were not particularly revealing. The oblate characteristics of the sample particulates could not be clearly resolved by the SEM after the conducting layer was added to the surface.

It is important at this time to make a point concerning the oblate shape of the particulates of the samples. In a recent dissertation [3.6], similar samples, prepared on silicon substrates, were described. For these samples a technique known as "shadow casting" was used to determine the particle shape. Through this technique, it was clearly shown that the particles were of oblate shape. It was not possible to use the shadow casting technique with the present samples due to the nonconducting quartz substrates. The basis for the assumption of the oblate characteristics of the particulates was the similarity of the two sample preparation techniques and the optical absorption results which are consistent with absorption by oblate spheroidal particles. The results indicate that the use of quartz instead of silicon as a substrate had little effect upon the formation of oblate spheroidal islands by the heating process, the bonding of silver to quartz and to silicon being roughly the same.

For oblate spheroidal islands formed on the quartz substrate, the orientations of all the spheroids' axes will be the same. As the micrograph in Figure 3-1 shows, the silver islands all have very nearly circular cross sections as viewed from normal incidence. For spheroidal islands, all the major axes would be aligned parallel with the plane of the substrate while the minor axes would then be perpendicular to the substrate.

Electron micrographs were taken of the sample when viewed at normal incidence. From these micrographs, much quantitative information such as the particle size distribution, average center-to-center separation, and particle density was determined. To obtain this information, the electron micrograph was mounted on the surface of an Orthoplex Coordinate Sensor [3.7]. The sensor surface is pressure sensitive and will record the x and y coordinate of a point when it has been depressed by a stylus. The coordinates of two points along the edges but on opposite sides of each particle were fed into the computer. From these coordinates, the average particle size and average center-to-center separation were calculated with the aid of a FORTRAN program [3.8]. For the samples used here, the average particle major axis was 60 nm with a typical center-to-center distance of 110 nm. From this, the average particle density is calculated to be $<\sim 83>$ particles/square micron. The particle size distribution histogram and particle spacing histogram are shown in Figures 3-2 and 3-3.

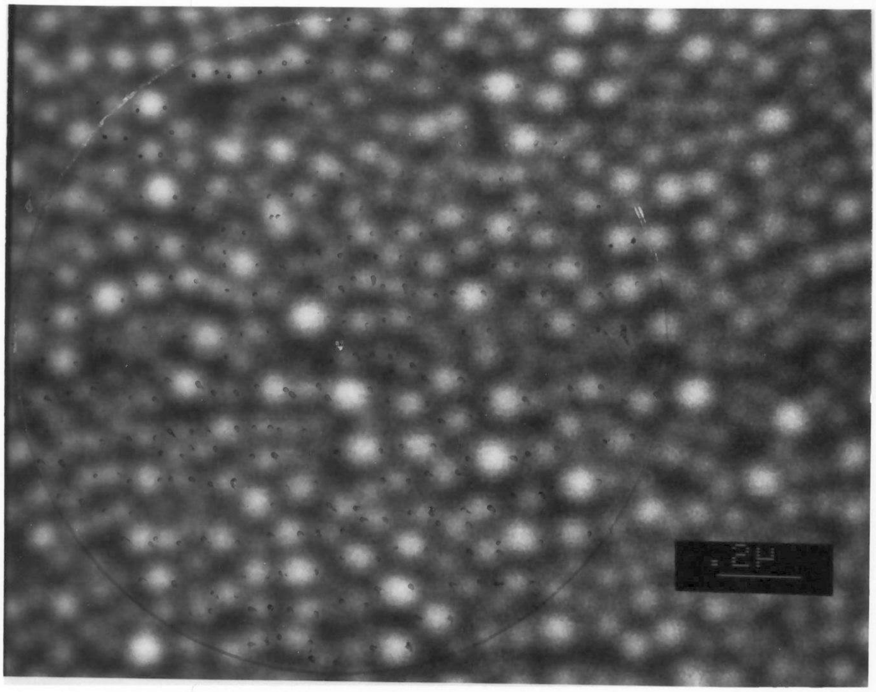

Figure 3-1. Electron micrograph of the sample surface. The view is along the surface normal. Note the scale bar in the lower right hand corner has a length of 20 nm.

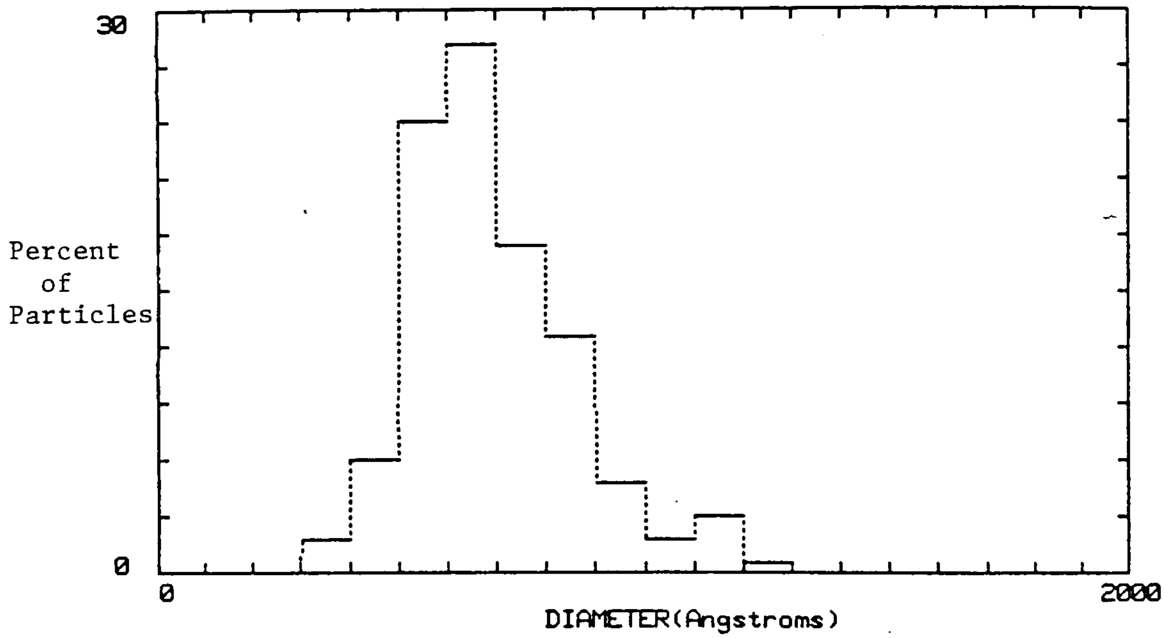

Figure 3-2. Histogram showing particle size distribution. These are obtained from micrographs such as the one in Figure 3-1.

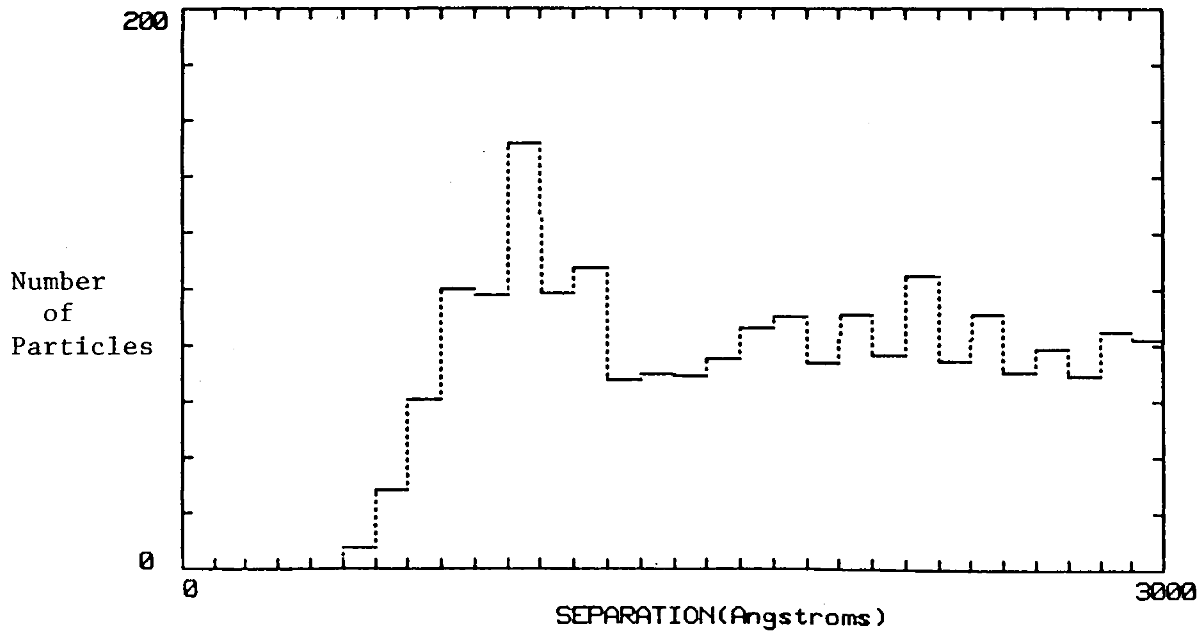

Figure 3-3. Histogram showing center-to-center particle separation distribution.

B. EXPERIMENTAL APPARATUS

All experimental optical data were taken on a CARY RECORDING SPECTROPHOTOMETER (Model 14R, Serial 64) [3.9]. The CARY displays directly, upon a strip chart recorder, the optical absorbance of the sample. The optical absorbance is defined as

$$\text{Absorbance} = \log_{10}(I_0/I_t) \, , \qquad (3\text{-}1)$$

where I_0 is the intensity of the light incident on the sample and I_t is the transmitted intensity.

The CARY has two chambers, these being referred to as the sample and reference chambers. A beam of monochromatic light is split into two beams of equal intensity, one of which passes through the reference chamber while the other passes through the sample chamber. The two beams are alternately chopped before entering the chambers. After leaving the chambers, both beams fall upon the same photomultiplier tube. Through a system of relay switches, the CARY compares the signal generated by the intensity of each of the two beams.

For all data taken in the present experiment, a clean quartz slide, cut from the same plate as the sample slide and cleaned in a similar manner, was placed in the reference beam. A sample, such as the one described earlier in Section 3A, was placed in the sample beam. The absorbance is then proportional to the ratio of the intensity of the beam passing through the quartz slide (reference) to the intensity passing through the sample slide. The presence of the quartz slide in the reference beam subtracts away from the displayed absorbance most of the optical effects of the quartz substrate. The displayed data are then due primarily to the presence of silver spheroids in the sample beam.

One of the more important aspects of this study is the angular dependence of the absorbance. In order to study this aspect, sample mounts were constructed that would fit into both the reference and sample chambers. The mounts allow one to vary the angle the quartz slide makes with the incident beam. The sample mounts were constructed by mounting an ORIEL 3 Inch Precision Rotator [3.10] onto an aluminum base that was milled to fit the sample or reference chamber. The slides were then mounted onto the Rotator and the Rotator adjusted to the desired angle. The sample mounts allow one to set the angle to within one degree.

The angular uncertainties were somewhat larger than one degree. This was due to the effect of the focusing of the reference and sample beams onto the slides. This source of error in the angle of incidence was measured to be about five degrees.

The CARY also allowed the user to choose a scan rate from 0.5 A/sec to 500 A/sec. In this experiment, a scan rate of 5 A/sec was used. The strip chart flow rate was set at two inches per minute.

The control of the polarization of the incident beams was an important part of this experiment. A plastic polaroid technical filter was mounted in front of the entrance windows of both the sample and reference chambers. The polaroid filters and rotatable sample mounts enabled the user to control the orientation the incident electric fields made with respect to the spheroids' axes. The conventional labelling of the polarization directions was used. Electric fields that are perpendicular to the plane of reflection are referred to as being s-polarized while electric fields that are contained in the plane of reflection are p-polarized.

The reference and sample slides were situated on the rotating mounts such that s-polarized incident fields would always lie parallel to the plane of the slide. This was true regardless of the angle the incident beam made with the slide. For p-polarization then, the electric fields lie parallel to the plane of the slide for normally incident beams just as in s-polarization. However, the perpendicular component of the p-polarized electric fields increases as the angle of incidence is increased. Figure 3-4 is a diagram of a typical sample and its orientation relative to the two directions of polarization.

C. DIGITIZING THE DATA

The CARY displayed the data upon a strip chart recorder. In order to make the comparison of the data and theory easier, the absorbance spectra were digitized from the strip chart recording. This was accomplished with the aid of the coordinate sensor mentioned earlier. The x and y coordinates of the digitized spectra were recorded and then converted into the corresponding values of wavelength and absorbance and stored in a designated file.

To make the analysis of the data easier, the data files were reformatted to contain the absorbance value at equal increments of the wavelength. This was easily done with the aid of a FORTRAN program [3.11]. The program fit a spline function between the existing data

ORNL-DWG 83-15081

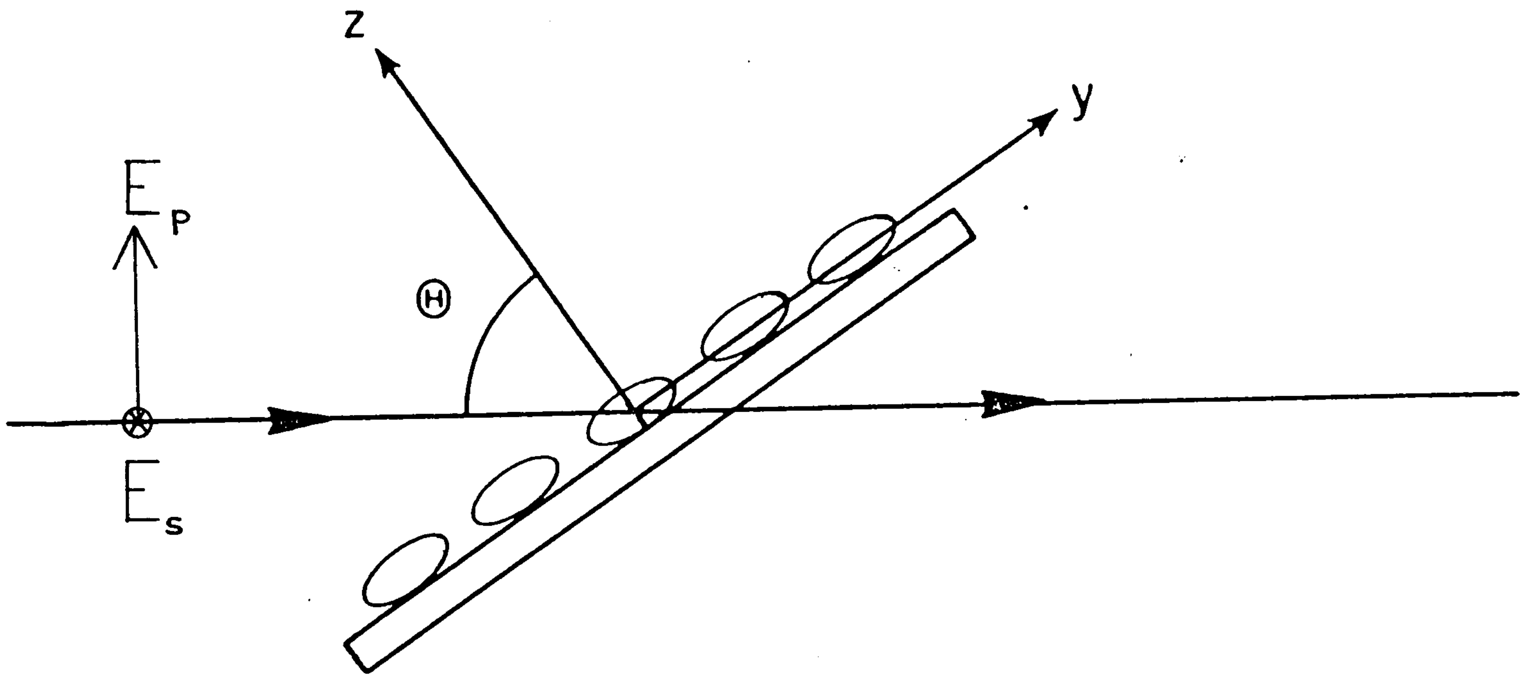

Figure 3-4. Illustration of the sample orientation relative to incident beam and electric fields.

points and then stored in a designated file a list of values of the wavelength and absorbance. The program also enabled the increment in the value of the wavelength to be set at 10 Angstroms. This process enabled the location of the maxima in the absorbance to be determined more easily. The data being stored in this form also allowed one to subtract one set of data points from another set of data points with little difficulty. As will be seen later, this capability proved to be very useful when analyzing the data.

CHAPTER IV

RESULTS AND ANALYSIS

In Chapter II, it was shown that the electrodynamic dipole cross section for a silver oblate spheroid has wavelength, polarization and angular dependencies which are determined primarily by its shape and bulk optical properties. In Chapter III, a technique for producing a collection of these spheroids was described along with techniques for analyzing experimental optical absorbance measurements made on the spheroids. In the present chapter, it is shown how the cross section can be related to the optical absorbance. The experimental results are then compared to numerical theoretical calculations of absorbance with favorable results.

A. RELATING THE CROSS SECTION TO THE ABSORBANCE

The cross sections, derived earlier in Chapter II, can be related to the optical absorbance in a straightforward manner. Let the intensity of the light falling upon the sample be denoted as I_0. Upon reaching the sample, the incident light is either transmitted through the sample, scattered by one or more of the spheroids or absorbed by one of the spheroids. Mathematically, this is expressed as

$$I_0 = I_t + I_s + I_a \tag{4-1}$$

where I_t, I_s and I_a represent the transmitted, scattered and absorbed intensities, respectively. Algebraically manipulating Eq. (4-1), one arrives at

$$\frac{I_0}{I_t} = \frac{1}{1 - \frac{I_s}{I_0} - \frac{I_a}{I_0}} \tag{4-2}$$

I_s/I_0 is the fraction of the incident light that is scattered into all solid angles. This is related to the single spheroid scattering cross section as

$$\frac{I_s}{I_0} = N\,\sigma_{sca} \tag{4-3}$$

where N is the number of spheroids per unit area. Similarly, for the absorption cross section, the relation is given by

$$\frac{I_a}{I_0} = N\,\sigma_{abs}\ . \tag{4-4}$$

Equation (4-2) then becomes

$$\frac{I_0}{I_t} = \frac{1}{1 - N\,\sigma_{total}}$$

where the total cross section, as defined earlier in Eqs. (2-42a) and (2-42b), has been used. The optical absorbance is then related to the total cross section as

$$\text{Absorbance} = \log_{10}\left(\frac{I_0}{I_t}\right) = \log_{10}\left(\frac{1}{1 - N\,\sigma_{total}}\right) . \qquad (4\text{-}5)$$

In deriving Eq. (4-5), the assumption has been made that none of the scattered light reaches the detector. The detector is placed behind the sample as shown in Figure 4-1. It measures the intensity of the light falling upon it, independent of whether the light was transmitted or scattered. To account exactly for the scattered intensity reaching the detector, one would need to calculate the scattering cross sections by integrating Eqs. (2-47a) and (2-47b) over all solid angle except that subtended by the detector. The solid angle subtended by the detector was measured to be about $\pi/10$ steradian. Since this is only 2.5% of the total solid angle, it was felt that neglecting the light scattered directly into the detector would be a reasonable approximation. An exact calculation was made for s-polarization involving the integration of the differential scattering cross section, Eq. (2-47a), over all solid angle but the detector. The only difference was that the factor of $8\pi/3$ in the scattering cross section turned out to be 8.03 in the exact cross section. This difference is small enough so that neglecting the light scattered directly into the detector is an adequate approximation.

B. EXPERIMENTAL RESULTS

The CARY, modified with the sample mounts mentioned earlier, is capable of measuring the optical absorbance for all angles of incidence up to around 70° throughout the near ultraviolet and visible spectrums.

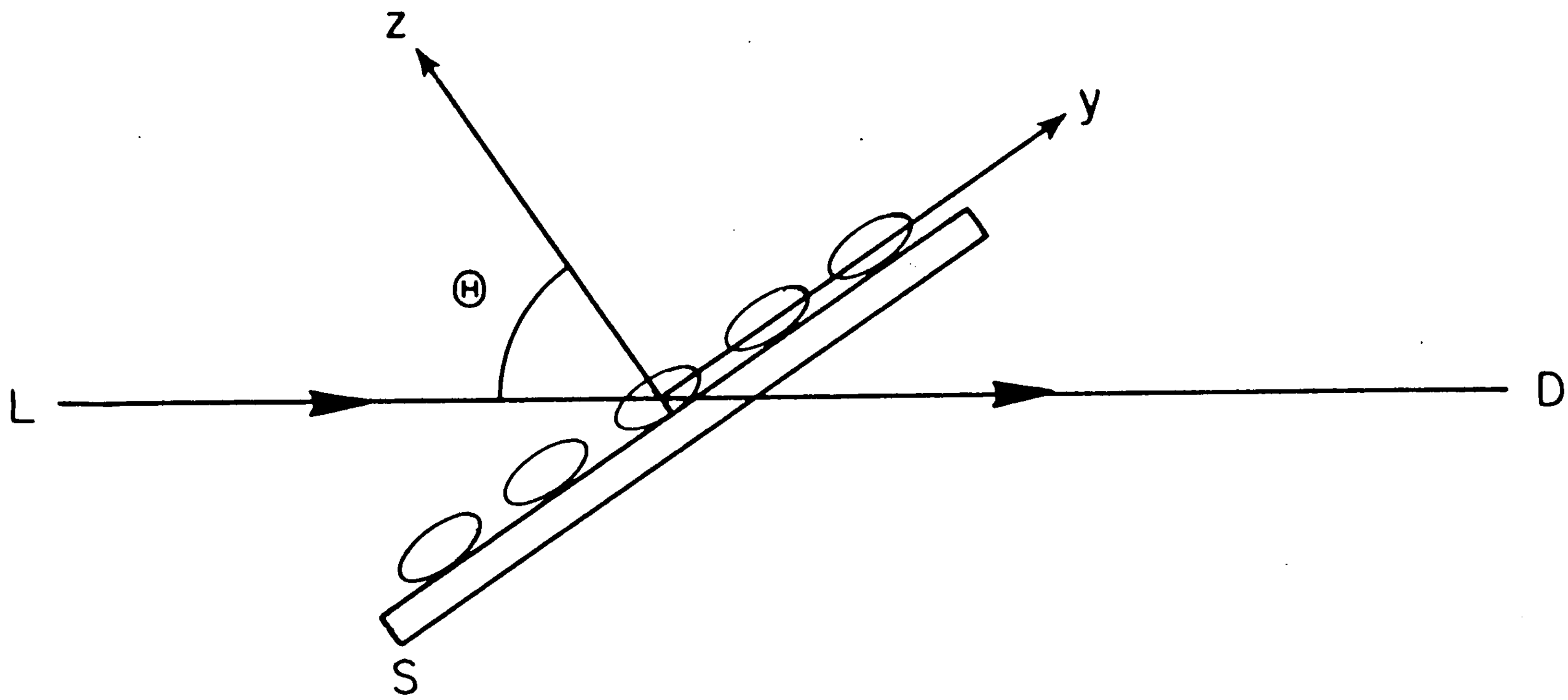

Figure 4-1. Illustration of the sample orientation. L is the light source; D is the detector; S is the sample and Θ is the angle of incidence.

From the plots of the cross sections presented earlier, it is seen that most of the interesting details concerning the scattering and absorption of light by silver spheroids is contained within the wavelength region of 300 nm to 500 nm. From Eqs. (2-48a) and (2-48b), it is seen that the cross sections for both polarizations (s and p) could differ greatly for nonnormal angles of incidence. In an effort to observe this angular dependence, experimental optical absorbance measurements were made at angles of 0°, 45° and 70°. Both polarizations of incident light were used in the wavelength region from 300 nm to 500 nm. The samples were those described in Section 3A.

The digitized experimental data are shown in Figures 4-2 and 4-3. Figure 4-2 is the data for s-polarization at the labelled angles of incidence. Figure 4-3 is for p-polarization at the same angles of incidence. In all data taken, there was a slight peak or shoulder around the 354 nm region. From the experimental bulk optical data, it is found that this occurs for frequencies, ω, where Re $\varepsilon(\omega) \approx -2$. It was shown, in Figure 2-4 on page 25, that $\varepsilon_{1m}(in_0)$ converges to -2 as the shape approaches that of a sphere. It is therefore assumed that the slight peak or shoulder in this particular region ($\approx$354 nm) is due to the presence of small silver spheres that are not resolved in the electron microscope or to a small portion of the particles, visible in the micrographs, that have very nearly spherical shapes. The scattering and absorption of light by spherical particles is a fairly well understood phenomenon and so, here, it is only a minor point of interest as a limiting case. The peak or shoulder due to the spherical particle contribution has thus been subtracted away from the experimental data.

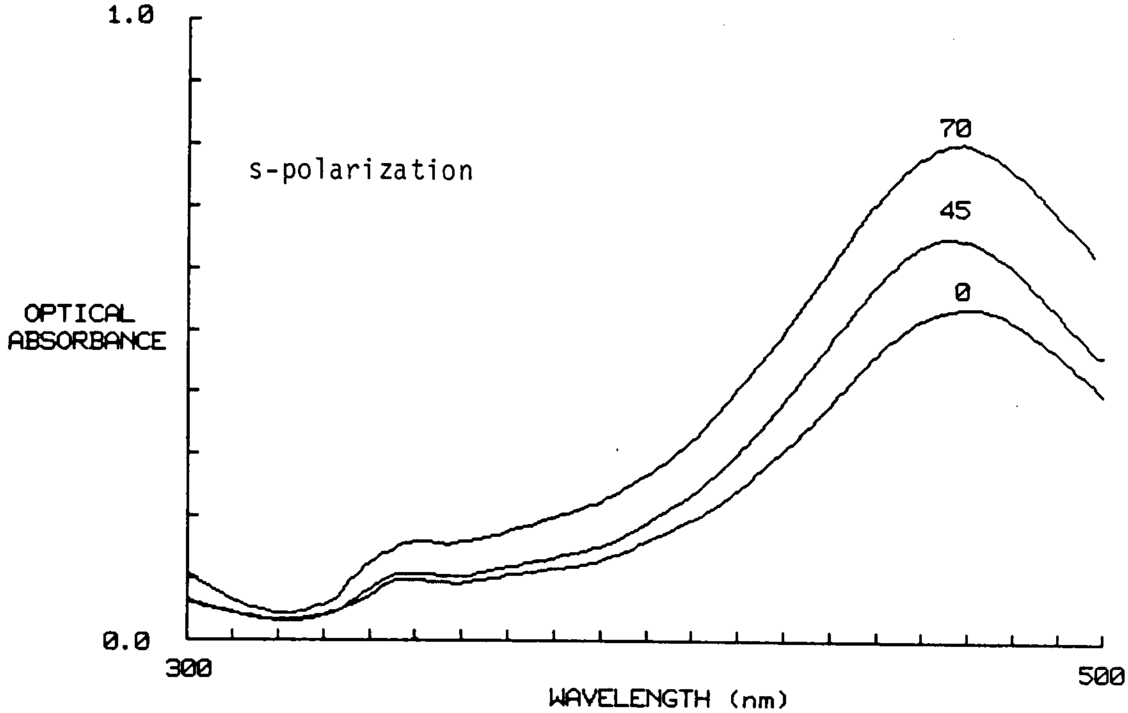

Figure 4-2. Optical absorbance as a function of wavelength for s-polarization. This is the raw experimental data. The curves shown are for 0°, 45°, and 70° angles of incidence.

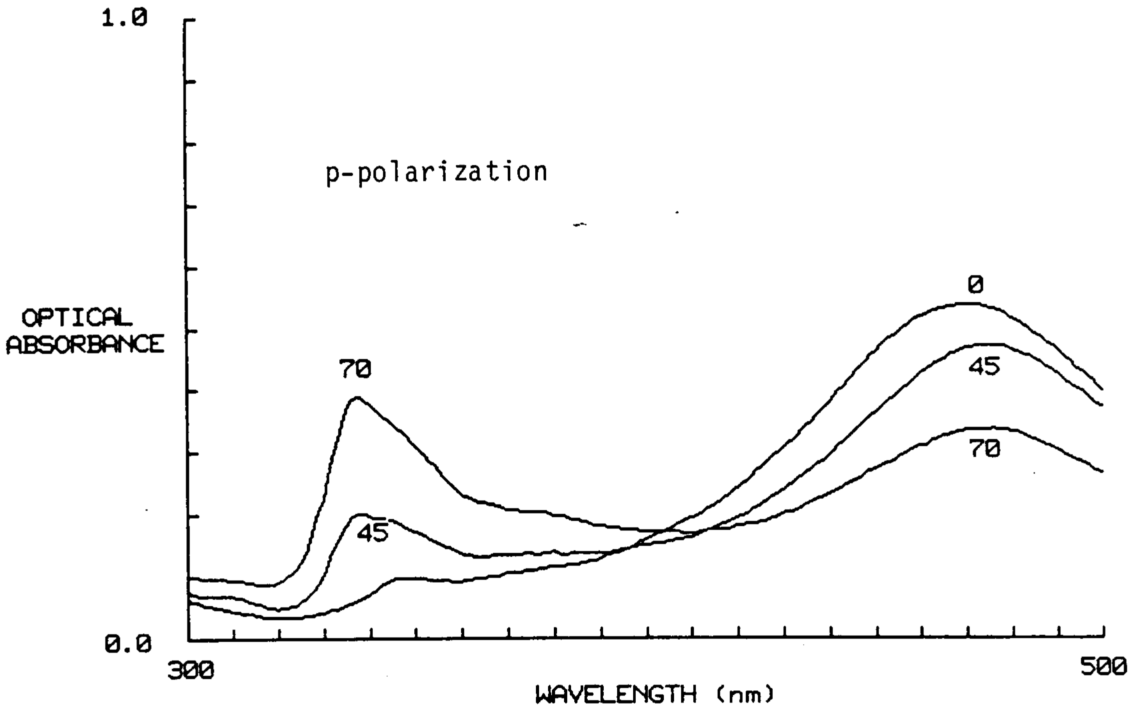

Figure 4-3. Optical absorbance as a function of wavelength for p-polarization. This is the raw experimental data. The curves shown are for 0°, 45°, and 70° angles of incidence.

To remove the spherical particle contribution, the short wavelength tail of the m=1 absorbance peak was extrapolated through the 354 nm region such that it passed through without a shoulder or peak. This is shown for the normal incidence data in Figure 4-4. This was done for all s-polarized data and then it was digitized again. It is in this form, shown in Figure 4-5, that the s-polarized data are compared with theory. The s-polarized data without the spherical contribution is then subtracted from the original s-polarized data. This difference was then subtracted from the p-polarized data. The resulting p-polarized data are shown in Figure 4-6 and it is in this form that it is compared with theory.

C. COMPARISON: THEORY AND EXPERIMENT

The theoretical absorbance for a single shape of silver spheroid was calculated and is shown in Figures 4-7 and 4-8. Figure 4-7 is for s-polarized incident light at the labelled angles of incidence while Figure 4-8 is for p-polarization. The number of particles per unit area was chosen so that the experimental and theoretical peak maxima would be the same height. Note that all the theoretical peaks are narrower than the experimental peaks. The additional peak broadening in the experimental data is attributed primarily to the presence of a distribution of particle shapes. The particles are known to have a distribution of sizes (see Figure 3-1 on page 41 and Figure 3-2 on page 42) and so it is reasonable to assume that there exists on the sample some distribution of particle shapes. Since there are no smaller peaks about the experimental peak, then there should exist on

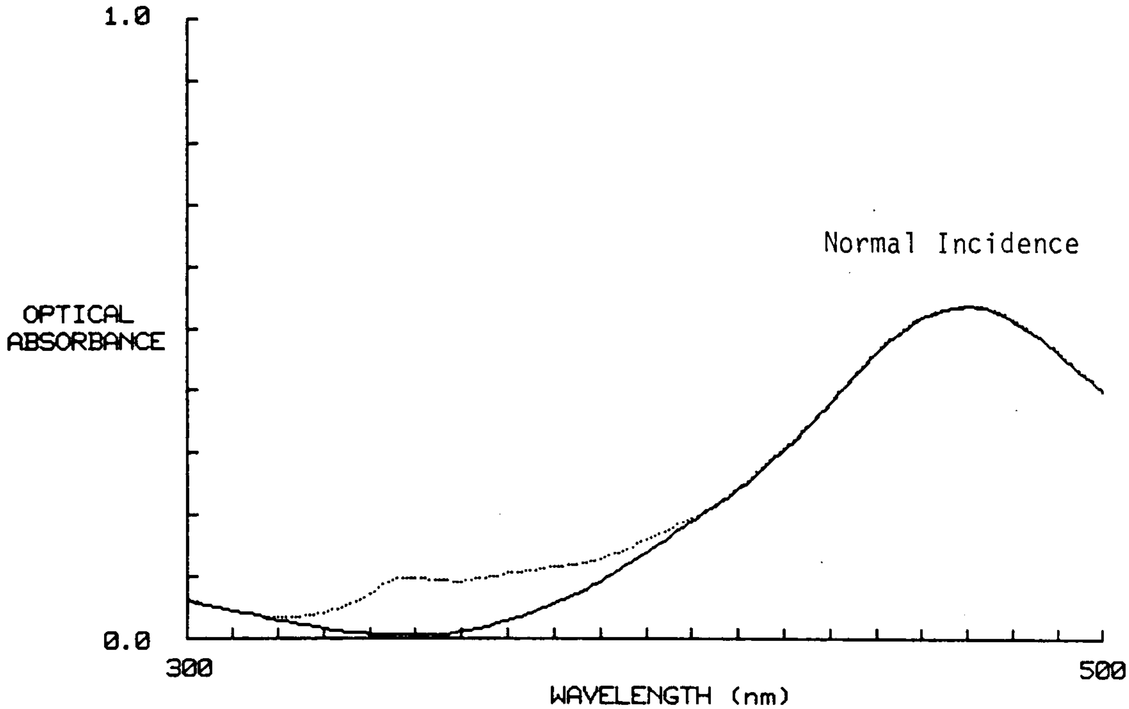

Figure 4-4. Optical absorbance as a function of wavelength for normal incidence; spherical particle subtraction. The dotted curve is the original experimental data. The solid curve is the same data but with the spherical particle contribution taken out.

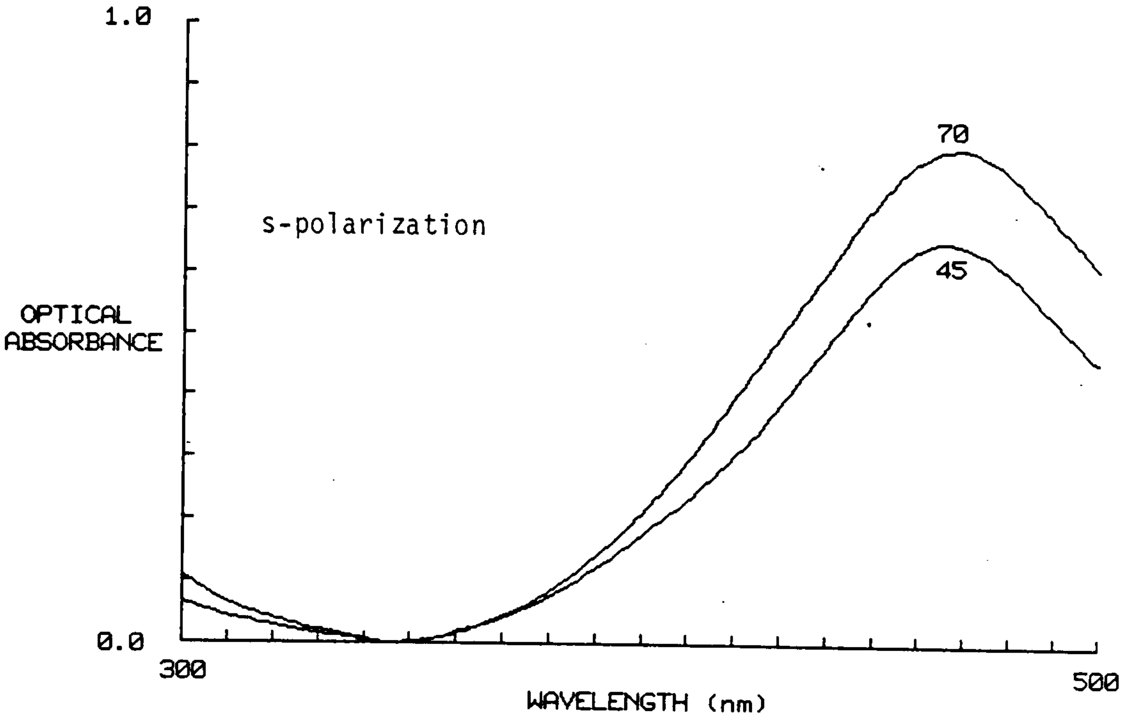

Figure 4-5. Optical absorbance as a function of wavelength for s-polarization at nonnormal angles of incidence. The spherical particle contributions have been taken out.

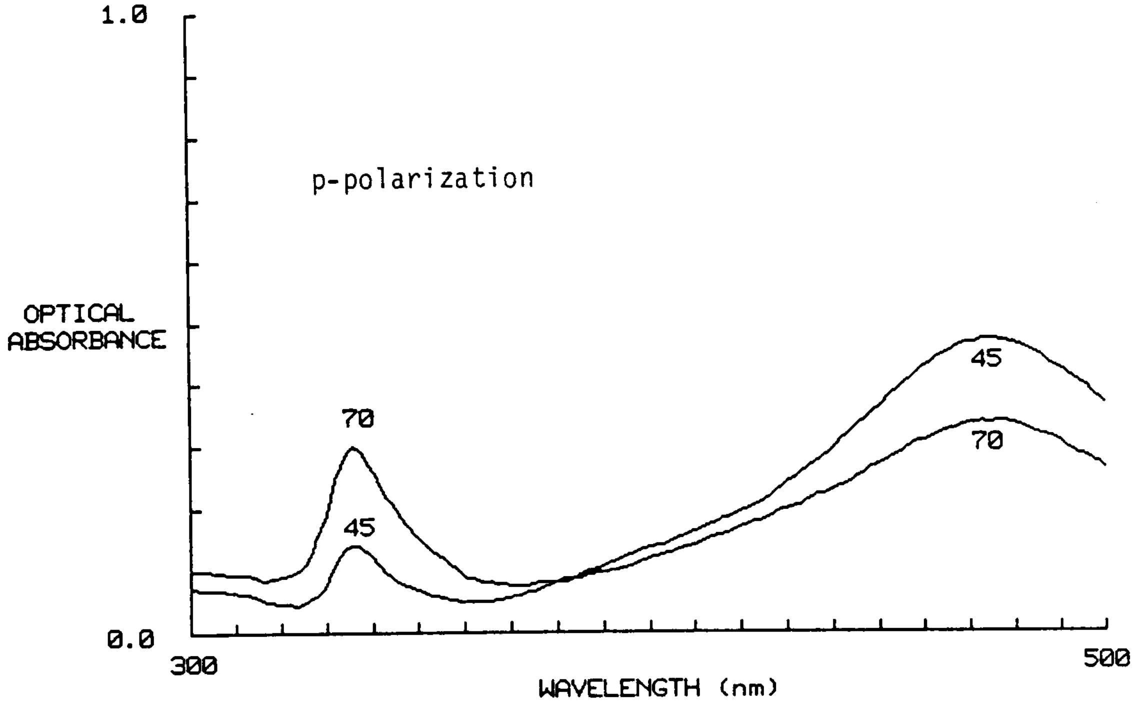

Figure 4-6. Optical absorbance as a function of wavelength for p-polarization at nonnormal angles of incidence. The spherical particle contribution has been taken out.

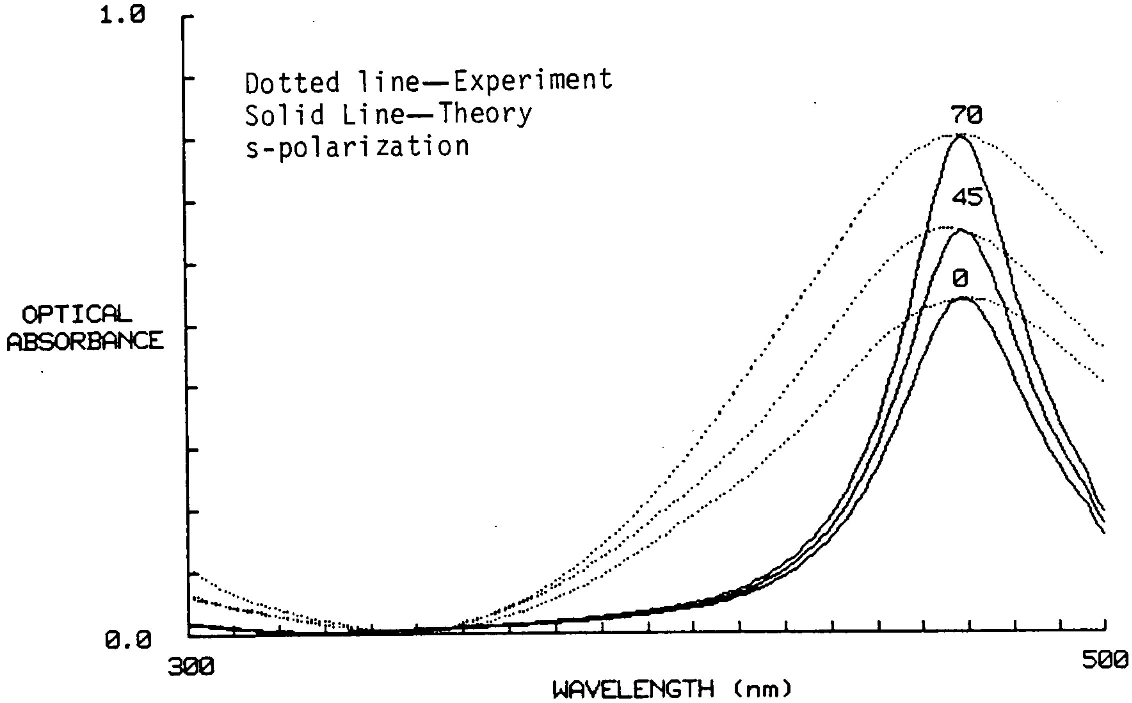

Figure 4-7. Optical absorbance as a function of wavelength for s-polarization. The dotted curves are experimental data. The solid curves are the best theoretical fit using a single minor-to-major axis ratio of 0.16.

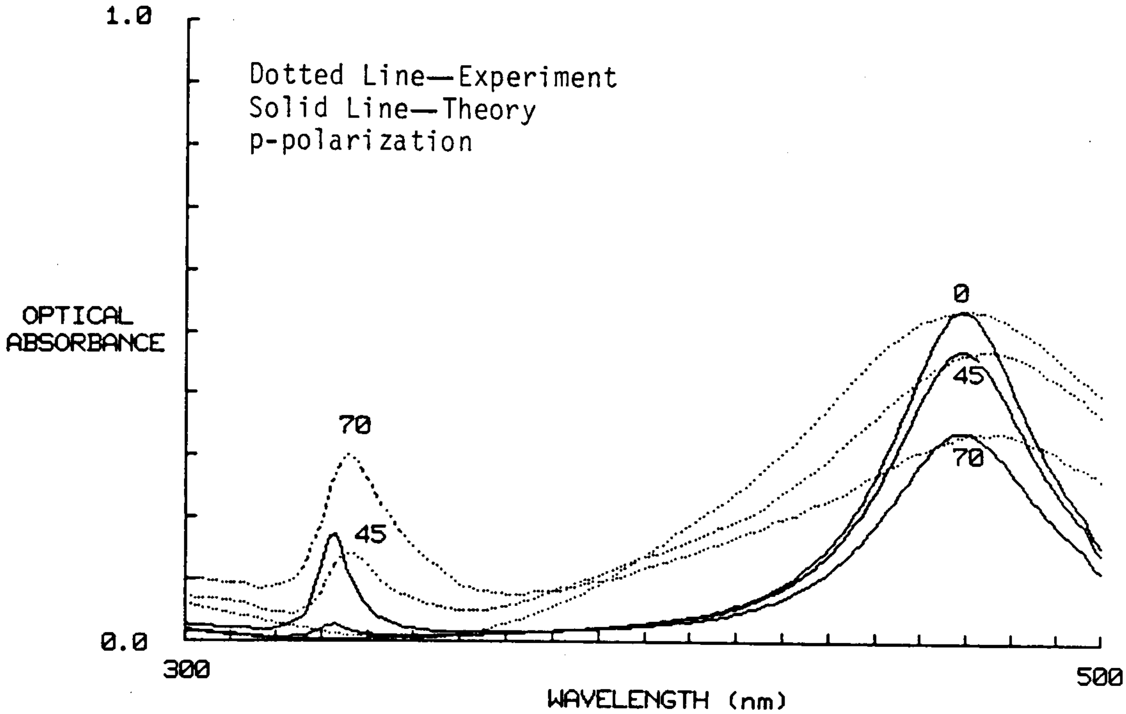

Figure 4-8. Optical absorbance as a function of wavelength for p-polarization. The dotted curves are experimental data. The solid lines are the best theoretical fit using a single minor-to-major axis ratio of 0.16.

the sample a distribution of shapes centered about a single shape of particle. Theoretically, this has been accounted for by calculating a weighted cross section for single particles with a Gaussian distribution [4.1] of shapes.

$$\sigma_{Wt} = \int_0^1 \sigma_{total} \frac{1}{\sqrt{2\pi}\, s} e^{-\frac{(R-R_0)^2}{2s^2}} dR \quad . \tag{4-6}$$

The weighted cross section shown above was numerically calculated with R_0, the central minor-to-major axis ratio, being chosen so that the location of the theoretical and experimental (m=1) peaks would be at the same wavelength. The variable s is the standard deviation in the Gaussian distribution of shapes. The value of s is varied to make the width of the theoretical absorbance match as closely as possible to the experimental data. The term $\frac{1}{\sqrt{2\pi}\, s}$ is a normalization factor. From Figure 2-7 (page 29), one can see that the position of the m=1 peak shifts significantly with small changes in the minor-to-major axis ratio while the m=0 peak shifts relatively little. This lends greatly to the broadness given the peaks by the Gaussian distribution in shapes. The theoretical absorbance for normal incidence is now much closer to the experimental absorbance at normal incidence as is shown in Figure 4-9. The theoretical absorbance was calculated using a central minor-to-major axis ratio of 0.155 and a standard deviation of 0.04. The constant N, chosen to match the peak height, is 8.2×10^{-7} particles/square Angstrom. This converts to 82 particles/

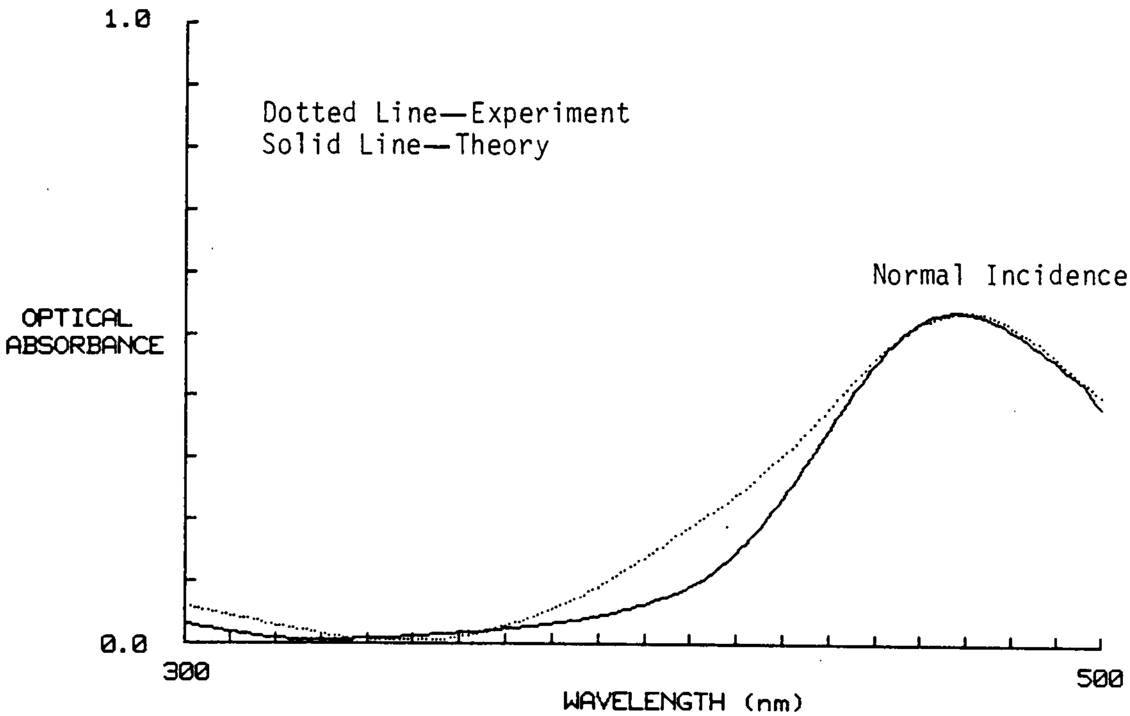

Figure 4-9. Optical absorbance as a function of wavelength for normal incidence. The dotted curve is the experimental data. The solid line is the best fit using a Gaussian distribution of minor-to-major axis ratios.

square micron which is very close to the measured particle density of 83 particles/square micron determined from the electron micrographs in Section 3A. Figures 4-10 and 4-11 are curves for the theoretical and experimental absorbance at nonnormal angles of incidence for each polarization. Again a central minor-to-major axis ratio of 0.155 along with a standard deviation of 0.04 was used for the shape distribution calculation. For the s-polarized calculations, nonnormal incidence, the constant N chosen to match the experimental peak heights turned out to be less than the measured particle density. The reason for this is thought to be that s-polarized light is partially reflected by the quartz slide in the reference chamber. This would reduce the measured value of I_0 and cause the measured absorbance values to be too small. The p-polarized calculations displayed a different effect. For p-polarized incident light, the constant N needed to fit the peak maxima was greater than the measured particle density. This increase is thought to be due to the presence of more particles in the beam caused by the converging and diverging path that the beam follows in passing through the slide.

In matching theory and experiment, the theoretical minor-to-major axis ratio was chosen so that the location of the longer wavelength peaks would coincide. This meant that most of the differences between the theoretical and experimental absorbance curves would lie in the location and height of the shorter wavelength (m=0) peak. One can see this in Figure 4-11. Probably a more accurate method of determining particle shape is to use the locations of both the m=0

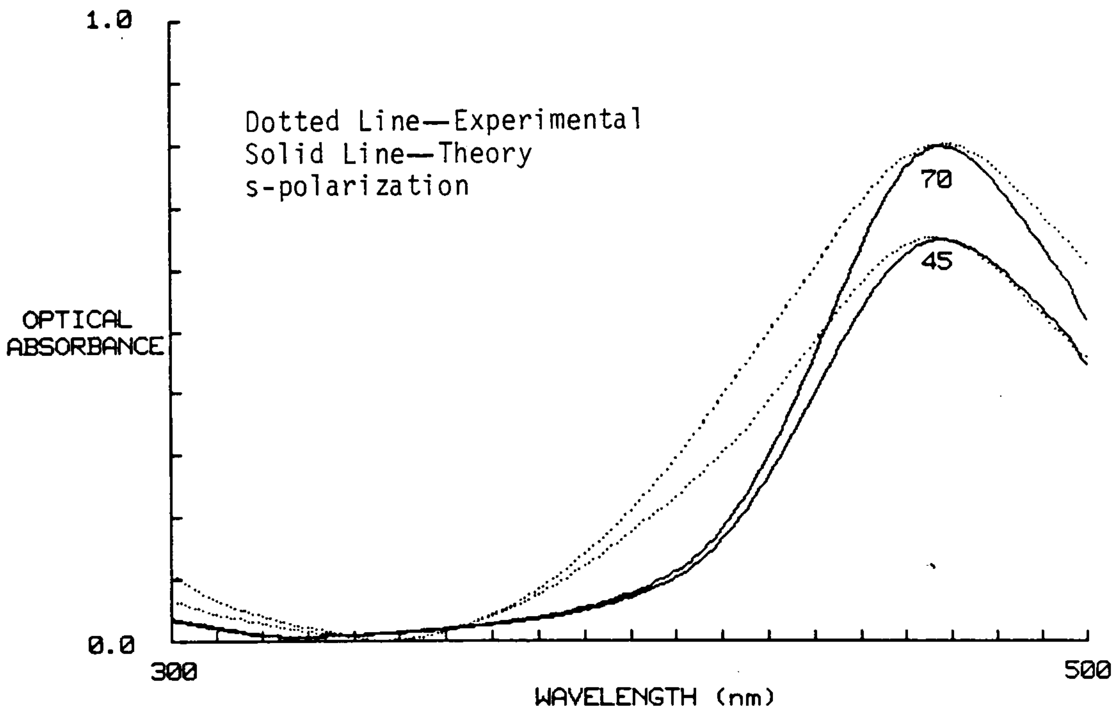

Figure 4-10. Optical absorbance as a function of wavelength for s-polarization at nonnormal angles of incidence. The dotted curves are the experimental data. The solid curves are the best theoretical fit using a Gaussian distribution in minor-to-major axis ratios.

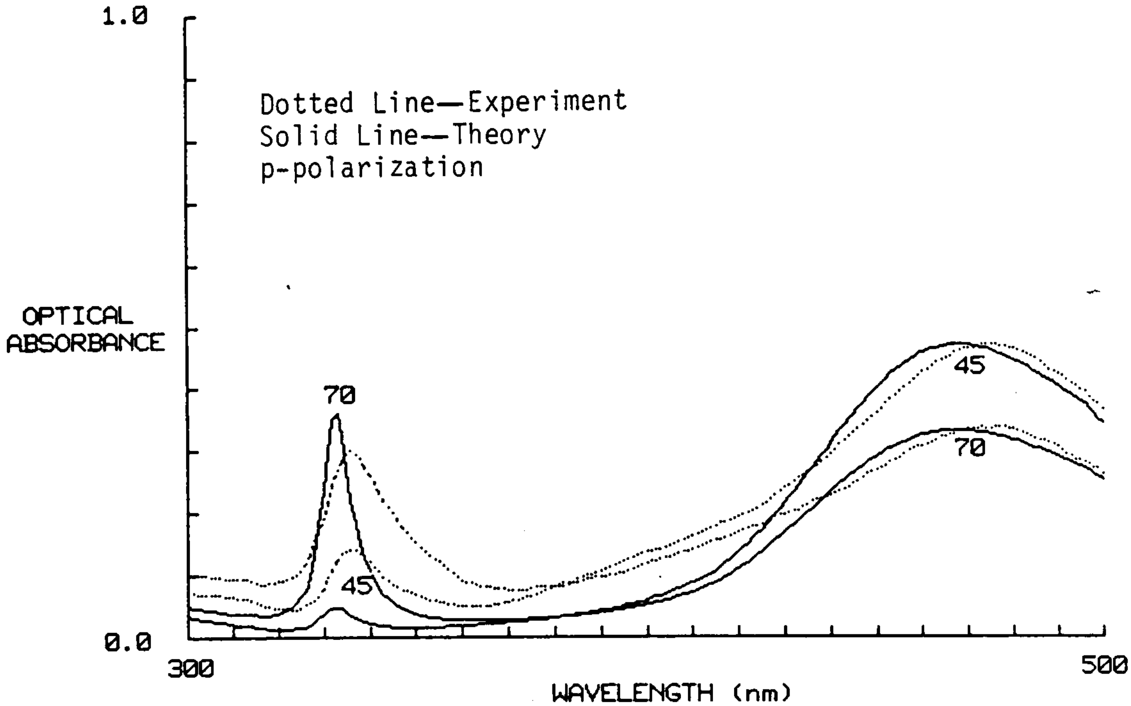

Figure 4-11. Optical absorbance as a function of wavelength for p-polarization at nonnormal angles of incidence. The dotted curves are the experimental data. The solid curves are the best theoretical fit using a Gaussian distribution in minor-to-major axis ratios.

and m=1 peaks. Figure 4-12 allows one to use the locations of both the experimental peaks to determine the most probable shape. In Figure 4-12, the experimental data has been placed below the graph from Figure 2-7. The experimental data is for p-polarization at 70°. To determine the shape from this figure, vertical lines are drawn from the experimental peaks extending through the curves in the figure immediately above. Ideally, a horizontal line could be drawn through the two intersection points which would intercept the shape axis at the appropriate value of the minor-to-major axis ratio. In practice, the best measurement of average shape is made by constructing a horizontal line from the shape axis that almost passes through the two points of intersection. This has been done in Figure 4-12 and the minor-to-major axis ratio determined in this manner is 0.2.

D. SOURCES OF ERROR

The presence of a quartz substrate may contribute some errors that are not completely compensated for by the use of the quartz slide in the reference beam. One effect may be that of an image charge in the substrate. The image charge is a dipole charge distribution on an oblate spheroid within the quartz but opposite in sign and smaller in magnitude than the distribution within the silver spheroid. The calculations of this effect [4.2] reveal that the effect of the image upon the absorbance is negligible until very small minor-to-major axis ratios are reached. The effect, if any, of the image on the absorbance is to shift the position of the m=1 peak to longer

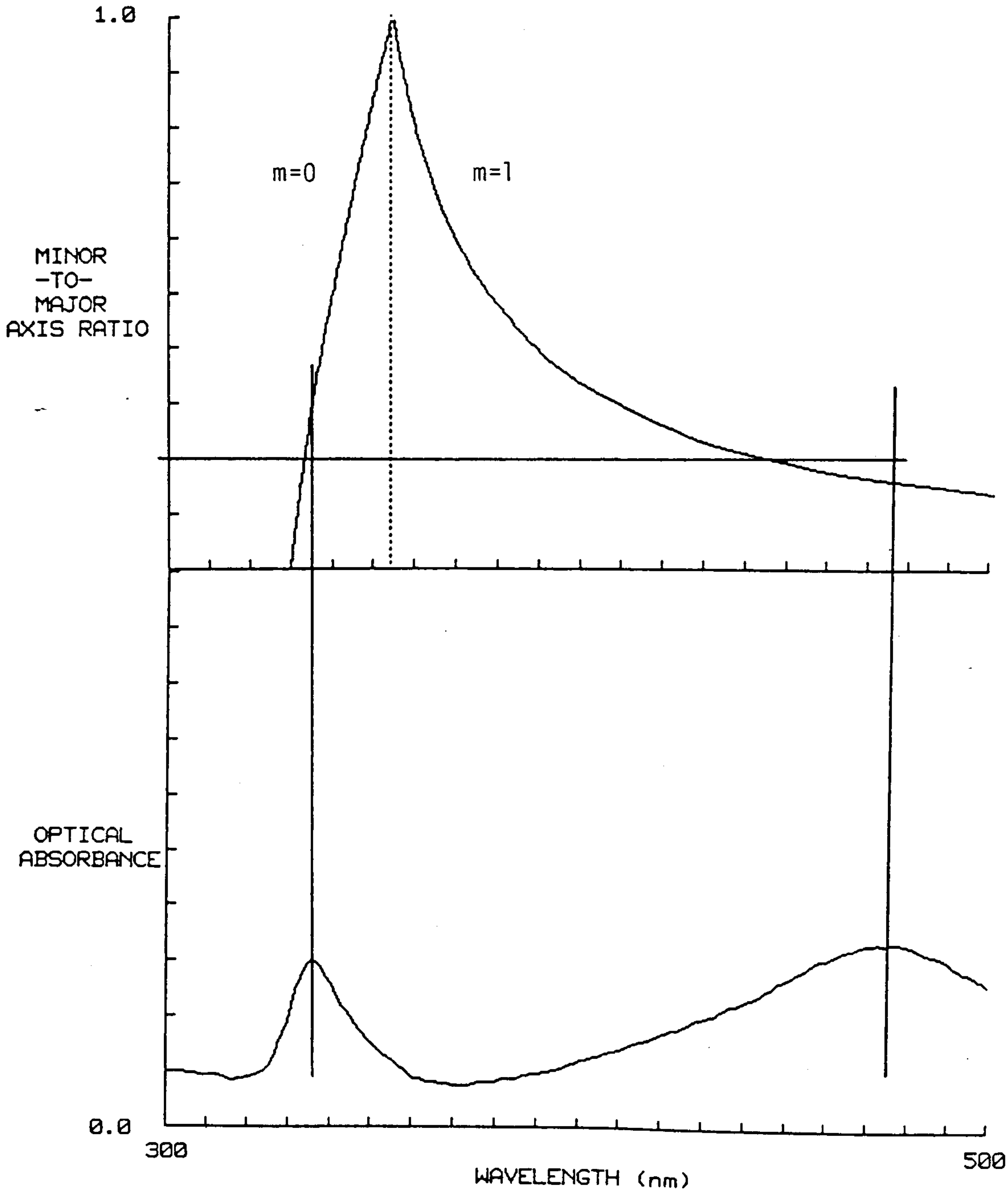

Figure 4-12. Two-peak method for determining the minor-to-major axis ratio. The bottom curve is experimental data for p-polarization at 70°. In the top figure are the curves from Figure 2-7 on page 29.

wavelengths (lower energies). If the effect is significant, then the actual minor-to-major axis ratio of the silver spheroids is slightly larger than the one used in matching the experimental and theoretical curves. With a larger minor-to-major axis ratio in the theoretical calculations, the position of the m=0 peak would be shifted to a longer wavelength and slightly better agreement between theory and experiment might be attained.

Another possible source of error is the bulk optical data used in the numerical calculations. An error in the real part of $\varepsilon(\omega)$ would produce an error in the position of the peaks and any error in the imaginary part would show up in the heights of the peak. For all calculations, the real and imaginary parts of the dielectric response were determined by a linear interpolation between the nearest two sets of values for $\varepsilon(\omega)$ given in the experimental data.

Any deviations in the average particle density or shape as a function of position on the slide would also produce some error. The slit width in the spectrophotometer is automatically varied by the instrument to allow for the spectral response of the photomultiplier tube. At various wavelengths, the slit width differs and so either more or less area of the sample slide is illuminated by the incident beam. Any variations with position on the slide of the average particle shape or average particle density would then produce some error. This type of error is thought to be small because the coloring of the sample slide appeared to be uniform when viewed by transmission and also there was no detectable difference in particle density as a function of position when the sample surface was viewed with a SEM.

E. CONCLUSIONS

Many workers (referenced in Chapter I) have studied the scattering and absorption of electromagnetic waves by various means. The uniqueness of the work presented here stems from the fact that the shape of the object can be quantitatively determined from simple measurements of optical absorption and scattering. The analysis requires that the bulk optical properties of the spheroid material be known in the region of interest. The theory, while somewhat long and algebraically tedious, is a straightforward calculation utilizing only classical electromagnetic theory. So long as the size of the scattering or absorbing object is small compared to the wavelength of the incident electromagnetic wave, the theory can be applied to any oblate spheroidal object. The theory can also be easily modified for the presence of an exterior dielectric.

Recently, samples such as the ones used in this work have been used as substrates in surface enhanced Raman scattering (SERS) experiments. It is believed that the electric field enhancements near the spheroid, which occur at the resonant frequencies, aid in producing a strong Raman signal. Oblate spheroids produce large electric field enhancements at different wavelengths depending upon their shape and composition. Thus, by selecting the spheroids' shape and material, SERS substrates may be tuned for maximum enhancement at selected wavelengths. Therefore, these substrates may prove to be very useful to workers in that field.

The theoretical section should be useful to future workers in any field who find that a spherical approximation will not adequately describe their problem. A more exact treatment may be found with the use of oblate spheroidal coordinates. As was shown by this work, asphericities can produce some of the more interesting and important aspects in the study.

REFERENCES

REFERENCES

CHAPTER I

[1.1]. Lord Rayleigh, Phil. Mag. XLIV, 28 (1897).

[1.2]. J. C. Maxwell-Garnett, Phil. Trans. Roy. Soc. London A204, 385 (1904).

[1.3]. G. Mie, Ann. Physik 25, 377 (1908).

[1.4]. R. Gans, Ann. Physik 47, 270 (1915); Ann. Physik 37, 881 (1912).

[1.5]. Erwin David, Z. Physik 114, 389 (1939).

[1.6]. Shigeo Yamaguchi, J. Phys. Soc. Japan 17 (7), 1172 (1962).

[1.7]. N. Emeric and A. Emeric, Thin Solid Films 1, 13 (1967).

[1.8]. David C. Skillman and Chester R. Berry, J. Chem. Phys. 48 (7), 3297 (1968).

[1.9]. John W. Little, Ph.D. Dissertation, The University of Tennessee, Knoxville, 1982.

CHAPTER II

[2.1]. William R. Smythe, Static and Dynamic Electricity, 3rd ed. (McGraw-Hill, New York, 1968), p. 168.

[2.2]. John W. Little, computer program COORD.FTN (Oak Ridge National Laboratory, Oak Ridge, TN).

[2.3]. Same as [2.1], p. 169.

[2.4]. Murray Spiegel, Mathematical Handbook of Formulas and Tables (Schaum's Outline Series, McGraw-Hill, New York, 1968), p. 125.

[2.5]. Same as [2.1], p. 159.

[2.6]. Phillip M. Morse and Herman Feshbach, Methods of Theoretical Physics (McGraw-Hill, New York, 1953), p. 1264.

[2.7]. John David Jackson, Classical Electrodynamics (Wiley and Sons, New York, 1975), p. 223.

[2.8]. Same as [2.1], p. 161.

[2.9]. Same as [2.7], p. 148.

[2.10]. John W. Little, Ph.D. Dissertation, The University of Tennessee, Knoxville, 1982.

[2.11]. R. H. Ritchie, J. C. Ashley, and T. L. Ferrell, Electromagnetic Surface Modes [Edited by A. D. Boardman] (Wiley and Sons, Ltd., Chichester, England, 1982), p. 124.

[2.12]. Same as [2.8].

[2.13]. Same as [2.7], p. 137.

[2.14]. Same as [2.7], p. 412.

[2.15]. Same as [2.7], p. 453.

[2.16]. Max Born and Emil Wolf, Principles of Optics, 5th ed. (Pergamon Press, Elmsford, New York, 1975), p. 33.

[2.17]. Same as [2.7], p. 454.

[2.18]. Same as [2.7], p. 271.

[2.19]. Same as [2.16], p. 659.

[2.20]. H. J. Hageman, W. Gudat, and C. Kunz, DESY Report No. SR-74/7, 1974 (unpublished).

[2.21]. Standard Mathematical Tables, 24th ed. (CRC Press, Cleveland, Ohio, 1976), p. 17.

[2.22]. H. C. van de Hulst, Light Scattering by Small Particles (Wiley and Sons, New York, 1957), p. 66.

[2.23]. Same as [2.7], p. 413.

[2.24]. Same as [2.4], p. 111.

[2.25]. Same as [2.4], p. 110.

CHAPTER III

[3.1]. Thorwald Anderson and C. G. Granqvist, J. Appl. Phys. 48, 1673 (1977).

[3.2]. General Electric type 101 or equivalent.

[3.3]. International Products Corporation, P.O. Box 118, Trenton, NJ 08601.

[3.4]. E. H. Sargent and Company, Chicago, IL, Model 506.

[3.5]. SEMCO Instruments Company, Limited, Ottawa, Canada.

[3.6]. John W. Little, Ph.D. Dissertation, The University of Tennessee, Knoxville, 1982.

[3.7]. Applied Physics Corporation, Pasadena, CA.

[3.8]. Oriel Corporation, 15 Market Street, Stamford, CT 06902.

[3.9]. Elographics, Inc., Oak Ridge, TN 37830.

[3.10]. R. J. Warmack, computer program SPLINE.FTN (Oak Ridge National Laboratory, Oak Ridge, TN, 1982).

CHAPTER IV

[4.1]. Herman T. Epstein, Elementary Biophysics Selected Topics (Addison-Wesley, Reading, MA, 1963), p. 5.

[4.2]. Same as [2.16], p. 40.

[4.3]. John W. Little (private communication).

APPENDIX B

[B.1]. Murray R. Spiegel, Mathematical Handbook of Formulas and Tables (Schaum's Outline Series, McGraw-Hill, New York, 1968), p. 128.

[B.2]. William R. Smythe, Static and Dynamic Electricity, 3rd ed. (McGraw-Hill, New York, 1968), p. 170.

[B.3]. Same as [B.1], p. 149.

[B.4]. Same as [B.2], p. 155.

[B.5]. Phillip M. Morse and Herman Feshbach, Methods of Theoretical Physics (McGraw-Hill, New York, 1953), p. 1265.

[B.6]. Same as [B.2], p. 156.

APPENDIX C

[C.1]. John David Jackson, Classical Electrodynamics, 2nd ed. (Wiley and Sons, New York, 1975), p. 767. Note that here the complex spherical harmonics have been replaced by the real spherical harmonics.

[C.2]. William R. Smythe, Static and Dynamic Electricity, 3rd ed. (McGraw-Hill, New York, 1968), p. 156.

[C.3]. Same as [C.1], p. 741.

[C.4]. Murray R. Spiegel, Mathematical Handbook of Formulas and Tables (Schaum's Outline Series, McGraw-Hill, New York, 1968), p. 24.

APPENDICES

APPENDIX A

RELATING CARTESIAN TO OBLATE SPHEROIDAL VARIABLES

In this appendix, the three cartesian variables, x, y and z are each related to the three oblate spheroidal variables η, μ and ϕ. The end result should be that given by Eqs. (2-3a) and (2-3c).

From Eq. (2-1), first let $x^2 + y^2 = r^2$ and after some manipulation, the relation becomes

$$z = a\eta\left(1 - \frac{r^2}{a^2(1 + \eta^2)}\right)^{1/2} . \tag{A-1}$$

Now, upon taking the derivative of z with respect to r in Eq. (A-1) one arrives at

$$\frac{dz}{dr} = \frac{r\eta}{a(1 + \eta^2)\left(1 - \frac{r^2}{a^2(1 + \eta^2)}\right)^{1/2}} \tag{A-2}$$

From Eq. (2-2) and again letting $x^2 + y^2 = r^2$ and solving the equation for z, one gets

$$z = a\mu\left(\frac{r^2}{a^2(1 - \mu^2)} - 1\right)^{1/2} . \tag{A-3}$$

Again, the derivative of z is taken with respect to r but this time in Eq. (A-3), so one gets

$$\frac{dz}{dr} = \frac{r\mu}{a(1 - \mu^2)\left(\dfrac{r^2}{a^2(1 - \mu^2)} - 1\right)^{1/2}} \tag{A-4}$$

Since the ellipses of Eq. (2-1) and the hyperbolas of Eq. (2-2) are required to be orthogonal, the derivative in Eq. (A-2) must equal the negative of the reciprocal of Eq. (A-4). Upon setting these equal and after some manipulation one gets

$$r^2\eta\mu = a^2(1 + \eta^2)(1 - \mu^2)\left(1 - \frac{r^2}{a^2(1 + \eta^2)}\right)^{1/2}\left(\frac{r^2}{a^2(1 - \mu^2)} - 1\right)^{1/2} . \tag{A-5}$$

From Eqs. (A-1) and (A-3) one can see that

$$\left(1 - \frac{r^2}{a^2(1 + \eta^2)}\right)^{1/2} = \frac{z}{a\eta} \tag{A-6}$$

and

$$\left(\frac{r^2}{a^2(1 - \mu^2)} - 1\right)^{1/2} = \frac{z}{a\mu} . \tag{A-7}$$

Upon substituting Eqs. (A-6) and (A-7) into Eq. (A-5) one gets

$$r^2 = z^2 \frac{(1 + \eta^2)(1 - \mu^2)}{\eta^2\mu^2} . \tag{A-8}$$

Upon taking the square of Eq. (A-1) and inserting the result into Eq. (A-8), one can manipulate the result to get

$$r = a(1 + \eta^2)^{1/2}(1 - \mu^2)^{1/2} . \tag{A-9}$$

The variable r may be related to x and y by the azimuthal angle ϕ. The relations are

$$x = r \cos \phi$$

and

$$y = r \sin \phi \ .$$

This leaves x and y in the form given in Eqs. (2-3a) and (2-3b) where

$$x = a(1 + \eta^2)^{1/2}(1 - \mu^2)^{1/2} \cos \phi \tag{2-3a}$$

and

$$y = a(1 + \eta^2)^{1/2}(1 - \mu^2)^{1/2} \sin \phi \ . \tag{2-3b}$$

To find the relation for z, refer back to Eqs. (2-1) or (2-2) and insert the relation for r found in Eq. (A-9) into either of these equations. After some manipulation one arrives at Eq. (2-3c)

$$z = a\,\eta\,\mu \ . \tag{2-3c}$$

APPENDIX B

SOLUTIONS TO LAPLACE'S EQUATION

Laplace's equation in oblate spheroidal coordinates is given by [B.1]

$$\nabla^2 V = \frac{1}{a^2(\eta^2 + \mu^2)} \left\{ \frac{\partial}{\partial \eta}\left[(\eta^2 + 1)\frac{\partial V}{\partial \eta}\right] + \frac{\partial}{\partial \mu}\left[(1 - \mu^2)\frac{\partial V}{\partial \mu}\right] + \frac{\eta^2 + \mu^2}{(1 + \eta^2)(1 - \mu^2)} \frac{\partial^2 V}{\partial \phi^2} \right\} = 0 \ . \tag{B-1}$$

The method of solution is the standard separation of variables technique. Upon inserting the potential as given by

$$V = F(\eta)G(\mu)J(\phi)$$

and dividing by the potential, Eq. (B-1) becomes

$$\left[\frac{(1 + \eta^2)(1 - \mu^2)}{\eta^2 + \mu^2}\right]\left\{\frac{1}{F}\frac{\partial}{\partial \eta}\left[(\eta^2 + 1)\frac{\partial F}{\partial \eta}\right] + \frac{1}{G}\frac{\partial}{\partial \mu}\left[(1 - \mu^2)\frac{\partial G}{\partial \mu}\right] + \frac{1}{J}\frac{\partial^2 J}{\partial \phi^2}\right\} = 0. \tag{B-2}$$

Note that the last term is dependent only upon the variable ϕ and thus it must separately equal a constant. Let the constant be $-m^2$, then the last term becomes

$$\frac{d^2 J(\phi)}{d\phi^2} = -m^2 J(\phi) \ . \tag{B-3}$$

Here the partial derivative is allowed to be a total derivative because it is a function of only the one variable ϕ. The solutions to Eq. (B-3) are [B.2]

$$J_{mp}(\phi) = \begin{cases} K_{mp} \cos(m\phi) & p = +1 \\ \\ L_{mp} \sin(m\phi) & p = -1 \end{cases} . \qquad \text{(B-4)}$$

Equation (B-2) can now be written as

$$\left[\frac{1}{F}\frac{\partial}{\partial\eta}\left((1+\eta^2)\frac{\partial F}{\partial\eta}\right) + \frac{m^2}{1+\eta^2}\right] + \left[\frac{1}{G}\frac{\partial}{\partial\mu}\left((1-\mu^2)\frac{\partial G}{\partial\mu}\right) - \frac{m^2}{1-\mu^2}\right] = 0 . \qquad \text{(B-5)}$$

Note that each of the terms in the large brackets is dependent only upon η or μ. Each term then must separately equal a constant; because their sum must be zero, one must be the negative of the other. Upon letting the constant be $\ell(\ell+1)$, Eq. (B-5) may be separated into two differential equations

$$\frac{1}{F}\frac{d}{d\eta}\left((1+\eta^2)\frac{dF}{d\eta}\right) + \frac{m^2}{1+\eta^2} = \ell(\ell+1) \qquad \text{(B-6)}$$

and

$$\frac{1}{G}\frac{d}{d\mu}\left((1-\mu^2)\frac{dG}{d\mu}\right) - \frac{m^2}{1-\mu^2} = -\ell(\ell+1) . \qquad \text{(B-7)}$$

The solutions to the differential equation (B-7) are the familiar Legendre polynomials [B.3]

$$G(\mu) = [A_{\ell m}P_{\ell m}(\mu) + B_{\ell m}Q_{\ell m}(\mu)] \ . \tag{B-8}$$

The solutions to the differential equation (B-6) are the Legendre functions of imaginary argument [B.2]

$$F(\eta) = [C_{\ell m}P_{\ell m}(i\eta) + D_{\ell m}Q_{\ell m}(i\eta)] \ . \tag{B-9}$$

The complete solution to Laplace's equation in oblate spheroidal coordinates is obtained by combining the solutions of Eqs. (B-4), (B-8) and (B-9)

$$V = \sum_{\ell=0}^{\infty} \sum_{m=0}^{\ell} \sum_{p=\pm 1} [C_{\ell m}P_{\ell m}(i\eta)+D_{\ell m}Q_{\ell m}(i\eta)][A_{\ell m}P_{\ell m}(\mu)+B_{\ell m}Q_{\ell m}(\mu)] \begin{pmatrix} K_{mp}\cos(m\phi) \\ \\ L_{mp}\sin(m\phi) \end{pmatrix} . \tag{B-10}$$

Upon applying the solutions to a spheroid, the potential must remain finite everywhere. Note that for $\beta = 0$ and $\beta = \pi$, $\mu = \pm 1$ and also that $Q_{\ell m}(\pm 1)$ approaches infinity at these points [B.4]. Therefore, the coefficients $B_{\ell m} = 0$. The remaining terms containing β and ϕ dependencies may be combined to form the real spherical harmonics $Y_{\ell mp}(\beta,\phi)$. This leaves the solutions as

$$V = \sum_{\ell=0} \sum_{m=0} \sum_{p=\pm 1} [C_{\ell mp}P_{\ell m}(i\eta) + D_{\ell m}Q_{\ell m}(i\eta)]Y_{\ell mp}(\beta,\phi) \ . \tag{B-11}$$

The real spherical harmonics are obtained from [B.5]

$$Y_{\ell mp}(\beta,\phi) = \left[\frac{(2-\delta_m^0)(2\ell+1)(\ell-m)!}{4\pi(\ell+m)!}\right]^{1/2} P_{\ell m}(\mu)(\delta_p^{+1}\cos(m\phi) + \delta_p^{-1}\sin(m\phi)) .$$

If the solutions are separated into interior and exterior solutions, one may write

$$V_{in} = \sum_{\ell=0}^{\infty} \sum_{m=0}^{\ell} \sum_{p=\pm1} [C_{\ell mp}P_{\ell m}(i\eta) + D_{\ell mp}Q_{\ell m}(i\eta)]Y_{\ell mp}(\beta,\phi) \qquad \text{(B-12a)}$$

and

$$V_{out} = \sum_{\ell=0}^{\infty} \sum_{m=0}^{\ell} \sum_{p=\pm1} [C'_{\ell mp}P_{\ell m}(i\eta) + D'_{\ell mp}Q_{\ell m}(i\eta)]Y_{\ell mp}(\beta,\phi) . \qquad \text{(B-12b)}$$

Again the condition that the potential must remain finite everywhere is applied. Note that $Q_{\ell m}(i0)$ approaches infinity [B.6], so that the coefficients $D_{\ell m} = 0$. Similarly, since $P_{\ell m}(i\eta_0)$ approaches infinity, the coefficients $C_{\ell m} = 0$. Finally, Eqs. (B-12a) and (B-12b) are written as

$$V_{in} = \sum_{\ell=0} \sum_{m=0} \sum_{p=\pm1} C_{\ell mp}P_{\ell m}(i\eta)Y_{\ell mp}(\beta,\phi) \qquad \text{(B-13a)}$$

and

$$V_{out} = \sum_{\ell=0} \sum_{m=0} \sum_{p=\pm1} D'_{\ell mp}Q_{\ell m}(i\eta)Y_{\ell mp}(\beta,\phi) . \qquad \text{(B-13b)}$$

The potential needs to be continuous at the surface of the spheroid so Eqs. (B-13a) and (B-13b) are written as

$$V_{in} = \sum_{\ell=0} \sum_{m=0} \sum_{p=\pm1} A_{\ell mp}Q_{\ell m}(i\eta_0)P_{\ell m}(i\eta)Y_{\ell mp}(\beta,\phi)$$

$$V_{out} = \sum_{\ell=0} \sum_{m=0} \sum_{p=\pm 1} B_{\ell mp} P_{\ell m}(i\eta_0) Q_{\ell m}(i\eta) Y_{\ell mp}(\beta,\phi) \ .$$

This is the general form for the potential, both inside and outside the spheroid, as is given in Eqs. (2-7a) and (2-7b) of Chapter II.

APPENDIX C

DERIVATION OF THE TOTAL CROSS SECTION

This appendix fills in the details between Eq. (2-37) and Eqs. (2-42a) and (2-42b). Only the important steps are given here; the purely algebraic steps are deleted for brevity.

The numerator of Eq. (2-37) will simplify to

$$- \frac{c}{8\pi} \mathrm{Re}[(\underset{\sim}{E}_0 \cdot \underset{\sim}{E}^*_{sca}) + (\hat{n} \cdot \hat{n}_0)(\underset{\sim}{E}_{sca} \cdot \underset{\sim}{E}^*_0) - (\hat{n} \cdot \underset{\sim}{E}^*_0)(\hat{n}_0 \cdot \underset{\sim}{E}_{sca})] \cdot \hat{n}\, da\ . \quad \text{(C-1)}$$

The scattered electric fields are given by Eq. (2-28). The unit vector in the direction of observation is $\hat{n}$ and is given in Eq. (2-39). The unit vector in the direction of propagation is $\hat{n}_0$ and is given in Eq. (2-39). The incident electric field takes on different forms depending upon the polarization. The form of the electric fields for both polarizations (s and p) is given in Eqs. (2-41a) and (2-41b). The total cross section is then obtained by dividing Eq. (C-1) by the incident power per unit area

$$\frac{P_{inc}}{\text{area}} = \frac{c}{8\pi} |E_0|^2 \quad \text{(C-2)}$$

and integrating over all solid angles. First, the integration is carried out for s-polarized incident fields. Upon making the required substitutions for $\underset{\sim}{E}_{sca}$, $\underset{\sim}{E}_0$, $\hat{n}$ and $\hat{n}_0$, the integral for the s-polarized total cross section can be shown to be

$$\sigma_{total}\Big|_{s\text{-}pol} = - \int Re\left[\frac{\omega^2}{c^2 r}\left\{e^{-ikr} e^{ikr(\hat{n}\ \hat{n}_0)} \alpha_x^*(1 - \sin^2\theta\ \cos^2\phi)\right.\right.$$

$$+ e^{ikr} e^{-ikr(\hat{n}\cdot\hat{n}_0)} \alpha_x(\sin\Theta\ \sin\theta\ \sin\phi - \cos\ \Theta\ \cos\theta$$

$$- 2\sin\Theta\ \sin^3\theta\ \cos^3\phi\ \sin\phi$$

$$\left.\left. + 2\cos\Theta\ \sin^2\theta\ \cos\theta\ \cos^2\phi)\right\}\right] da\ . \qquad \text{(C-3)}$$

This integral can be done rather easily if some substitutions are made. The plane wave expansion for $e^{\pm ikr(\hat{n}\cdot\hat{n}_0)}$ [C.1] in terms of real spherical harmonics and spherical Bessell functions is

$$e^{\pm ikr(\hat{n}\cdot\hat{n}_0)} = 4\pi \sum_{\ell=0}^{\infty} (\pm i)^{\ell} j_{\ell}(kr) \sum_{m=0}^{\ell} \sum_{p=\pm 1} Y_{\ell mp}(\theta,\phi) Y_{\ell mp}(\overline{\Theta},\Phi)\ . \qquad \text{(C-4)}$$

The coordinates r, θ and ϕ are the spherical coordinates of the wave with wave vector $\underset{\sim}{k}$. The angles $\overline{\Theta}$ and Φ are the polar and azimuthal angles of incidence. From Figure C-1, one can see that $\Phi = \pi/2$ and $\overline{\Theta} = \pi - \Theta$. The terms in Eq. (C-3) containing Θ and Φ are now recast in terms of the real spherical harmonics [C.2]. These are found to be

$$1 - \sin^2\theta\ \cos^2\phi = \frac{2}{3}\sqrt{4\pi}\ Y_{00}^{1}(\theta,\phi) + \frac{1}{3}\sqrt{\frac{4\pi}{5}}\ Y_{20}^{1}(\theta,\phi) - \frac{1}{6}\sqrt{\frac{12\pi}{5}}\ Y_{22}^{1}(\theta,\phi) \qquad \text{(C-5)}$$

$$\sin\theta\ \sin\phi = \sqrt{\frac{4\pi}{3}}\ Y_{11}^{-1}(\theta,\phi) \qquad \text{(C-6)}$$

$$\cos\theta = \sqrt{\frac{4\pi}{3}}\ Y_{10}^{1}(\theta,\phi) \qquad \text{(C-7)}$$

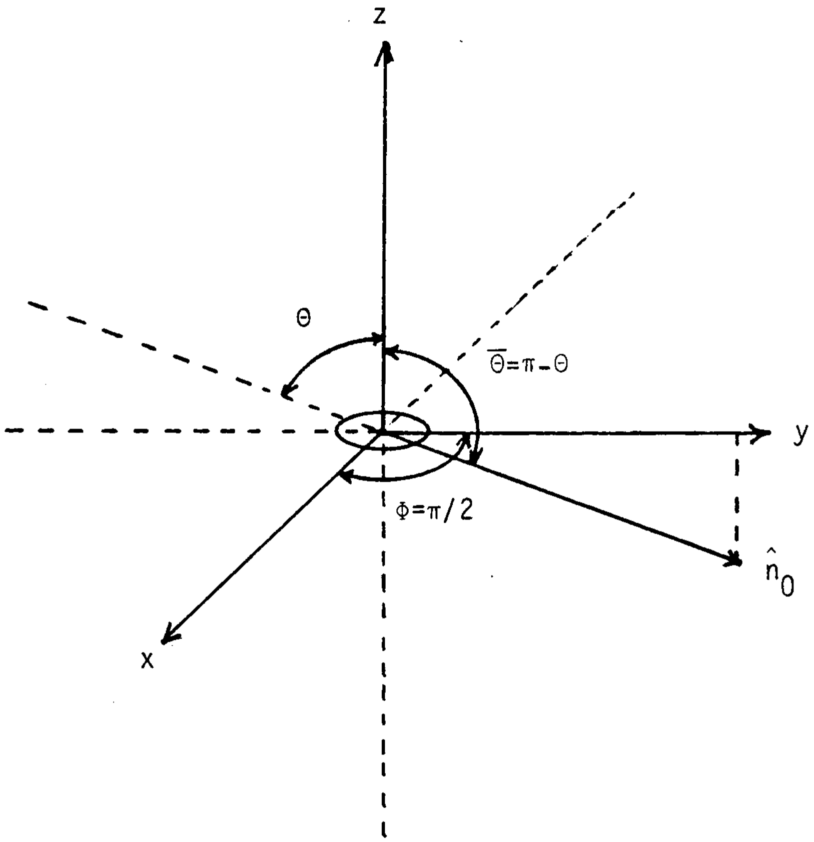

Figure C-1. This diagram shows the angles Θ and Φ that the unit vector $\hat{n}_0$ makes with respect to the z and x axes.

$$\sin^3\theta\ \cos^2\phi\ \sin\phi = \sqrt{\frac{1440\pi}{7}}\ \frac{1}{60}\ Y_{33}^{-1}(\theta,\phi) + \sqrt{\frac{4\pi}{3}}\ \frac{1}{5}\ Y_{11}^{-1}(\theta,\phi) - \sqrt{\frac{48\pi}{5}}\ \frac{1}{30}\ Y_{31}^{-1}(\theta,\phi) \tag{C-8}$$

$$\sin^2\theta\ \cos\theta\ \cos^2\phi = \sqrt{\frac{480\pi}{7}}\ \frac{1}{30}\ Y_{32}^{1}(\theta,\phi) - \sqrt{\frac{4\pi}{7}}\ \frac{1}{5}\ Y_{20}^{1}(\theta,\phi) + \sqrt{\frac{4\pi}{3}}\ \frac{1}{5}\ Y_{10}^{1}(\theta,\phi)\ . \tag{C-9}$$

The integrations may now be carried out rather easily because of the orthogonality of the spherical harmonics. Upon integrating, the first term turns out to be

$$\sigma_1 = -\mathrm{Re}\left\{\frac{4\pi\omega^2 r}{c^2}\ e^{-ikr}\alpha_x^*\ \left[(i)^0\ \frac{2}{3}\ \ 4\pi\ j_0(kr)Y_{00}^1\ (\overline{\Theta},\pi/2)\right.\right.$$
$$\left.\left. + (i)^2\ \frac{1}{3}\sqrt{\frac{4\pi}{5}}\ j_2(kr)Y_{20}^1\ (\overline{\Theta},\pi/2) - (i)^2\ \frac{1}{6}\sqrt{\frac{12\pi}{5}}\ j_2(kr)Y_{22}^1\ (\overline{\Theta},\pi/2)\right]\right\} \tag{C-10}$$

The spherical Bessel functions for $\ell=0$ and $\ell=2$ [C.3] are

$$j_0(kr) = \frac{\sin(kr)}{kr} \tag{C-11}$$

$$j_2(kr) = \frac{3\ \sin(kr)}{(kr)^3} - \frac{3\ \cos(kr)}{(kr)^2} - \frac{\sin(kr)}{kr} \tag{C-12}$$

If the integration is carried out over a sphere with a large enough radius, then terms with $1/r^2$ and $1/r^3$ will converge to zero. Thus upon letting $k = \omega/c$, Eq. (C-10) becomes

$$\sigma_1 = -\mathrm{Re}\left\{\frac{4\pi\omega}{c}\ e^{-i\ \frac{\omega r}{c}}\ \alpha_x^*\ \sin(\frac{\omega r}{c})\right\} \tag{C-13}$$

Similarly, Eqs. (C-6) and (C-4) are substituted into Eq. (C-3) to yield

$$\sigma_2 = -\mathrm{Re}\left[\frac{\omega^2 r}{c^2}\,\alpha_x e^{ikr}\,\sin\Theta\;4\pi(i)^1 j_1(kr)\sqrt{\frac{4\pi}{3}}\;Y_{11}^{-1}\;(\overline{\Theta},\pi/2)\right] \;. \qquad \text{(C-14)}$$

The ℓ=1 spherical Bessell function [C.3] is given by

$$j_1(kr) = \frac{\sin(kr)}{(kr)^2} - \frac{\cos(kr)}{(kr)} \qquad \text{(C-15)}$$

and Eq. (C-14) can be shown to be

$$\sigma_2 = -\mathrm{Re}\left[\frac{4\pi\omega}{c}\,\alpha_x e^{i\frac{\omega r}{c}}(i)\;\cos(\tfrac{\omega r}{c})\sin^2\Theta\right] \;. \qquad \text{(C-16)}$$

The third term in Eq. (C-3) is found in a similar manner to be

$$\sigma_3 = -\mathrm{Re}\left[\frac{4\pi\omega}{c}\,\alpha_x e^{i\frac{\omega r}{c}}(i)\cos(\tfrac{\omega r}{c})\cos^2\Theta\right] \;. \qquad \text{(C-17)}$$

The fourth and fifth terms in the integration of Eq. (C-3) will utilize the ℓ=3 term of the spherical Bessell function

$$j_3(kr) = \left[\frac{15}{(kr)^4} - \frac{6}{(kr)^2}\right]\sin(kr) - \left[\frac{15}{(kr)^2} - \frac{1}{(kr)}\right]\cos(kr) \;. \qquad \text{(C-18)}$$

Upon following the described technique, these terms are found after some manipulation to be zero.

$$\sigma_4 = \sigma_5 = 0 \;. \qquad \text{(C-19)}$$

The total cross section for s-polarization is obtained by taking the sum of Eqs. (C-13), (C-16), (C-17) and (C-19) and after some manipulation the cross section is found to be

$$\sigma_{\text{total}}\Big|_{s\text{-pol}} = -\text{Re}\left(\frac{4\pi\omega}{c}\left[\alpha_x^* \, e^{-i\frac{\omega r}{c}} \sin(\tfrac{\omega r}{c}) + i\alpha_x \cos(\tfrac{\omega r}{c}) e^{i\frac{\omega r}{c}}\right]\right) . \quad \text{(C-20)}$$

Now use Euler's equation [C.4] for $e^{\pm ikr}$, the cross section becomes

$$\sigma_{\text{total}}\Big|_{s\text{-pol}} = -\text{Re}\left(\frac{4\pi\omega}{c}\left[\cos(\tfrac{\omega r}{c})\sin(\tfrac{\omega r}{c})(\alpha_x^* - \alpha_x) - \sin^2(\tfrac{\omega r}{c})(i\alpha_x^*) + \cos^2(\tfrac{\omega r}{c})(i\alpha_x)\right]\right) . \quad \text{(C-21)}$$

By letting

$$\alpha_x = \text{Re}\ \alpha_x + i\ \text{Im}\ \alpha_x ,$$

$$\alpha_x^* = \text{Re}\ \alpha_x - i\ \text{Im}\ \alpha_x , \text{ and}$$

$$\alpha_x^* - \alpha_x = -2i\ \text{Im}\ \alpha_x ,$$

then Eq. (C-21) is shown to be

$$\sigma_{\text{total}}\Big|_{s\text{-pol}} = -\text{Re}\left(\frac{4\pi\omega}{c}\left[\sin(\tfrac{\omega r}{c})\cos(\tfrac{\omega r}{c})(-2i\ \text{Im}\ \alpha_x) - i\ \text{Re}\ \alpha_x(\cos^2(\tfrac{\omega r}{c}) - \sin^2(\tfrac{\omega r}{c})) - \text{Im}\ \alpha_x(\sin^2(\tfrac{\omega r}{c}) + \cos^2(\tfrac{\omega r}{c}))\right]\right) \quad \text{(C-22)}$$

Taking only the real part, the total cross section for s-polarization becomes

$$\sigma_{\text{total}}\Big|_{s\text{-pol}} = \frac{4\pi\omega}{c}\ \text{Im}\ \alpha_x . \quad \text{(C-23)}$$

The total cross section for p-polarization is found by following the same basic procedure. The incident electric field now takes the form given in Eq. (2-41b) and is substituted into Eq. (C-2) along with the relations used previously for $\underset{\sim}{E}_{sca}$, $\hat{n}$ and $\hat{n}_0$. The total cross section is then

$$\sigma_{total}\Big|_{p\text{-}pol} = -\int \mathrm{Re}\left[\frac{\omega^2}{c^2 r}\left[e^{ikr(\hat{n}\cdot\hat{n}_0)}\left(\alpha_y^{*}\cos^2\Theta\,(1 - \sin^2\theta\,\sin^2\phi)\right.\right.\right.$$

$$\left. + \alpha_x^{*}\sin^2\Theta\,\sin^2\theta - (\alpha_y^{*} + \alpha_z^{*})\sin\Theta\,\cos\Theta\,\sin\theta\,\cos\theta\,\sin\phi\right)$$

$$\left.\left. + e^{ikr}e^{-ikr(\hat{n}\cdot\hat{n}_0)}\left[-\alpha_y\cos\Theta\,\cos\theta + \alpha_z\sin\Theta\,\sin\theta\,\sin\theta\right]\right]\right] da. \tag{C-24}$$

Again the terms containing the angles θ and ϕ are recast into a form using the real spherical harmonics. These are found to be

$$(1 - \sin^2\theta\,\sin^2\phi) = \frac{2}{3}\sqrt{4\pi}\,Y^1_{00}(\theta,\phi) + \frac{1}{3}\sqrt{\frac{4\pi}{5}}\,Y^1_{20}(\theta,\phi) + \frac{1}{6}\sqrt{\frac{12\pi}{5}}\,Y^1_{22}(\theta,\phi) \tag{C-25}$$

$$\sin^2\theta = \frac{2}{3}\sqrt{4\pi}\,Y^1_{00}(\theta,\phi) - \frac{2}{3}\sqrt{\frac{4\pi}{5}}\,Y^1_{20}(\theta,\phi) \tag{C-26}$$

$$\sin\theta\,\cos\theta\,\sin\phi = \frac{1}{3}\sqrt{\frac{12\pi}{5}}\,Y^{-1}_{21}(\theta,\phi) \tag{C-27}$$

$$\cos\theta = \sqrt{\frac{4\pi}{3}}\,Y^1_{10}(\theta,\phi) \tag{C-28}$$

$$\sin\theta\,\sin\phi = \sqrt{\frac{4\pi}{3}}\,Y^{-1}_{11}(\theta,\phi)\ . \tag{C-29}$$

If Eqs. (C-25) through (C-29) are substituted into Eq. (C-24) along with the plane wave expansion of Eq. (C-4), then the integration can be carried out with relative ease because of the orthogonality of the spherical harmonics. The results, after integrating, contain the spherical Bessel functions for ℓ=0, 1 and 2. The forms for these are given in Eqs. (C-11), (C-15) and (C-12), respectively. After considerable manipulation, the results of the integrations are found to be

$$\sigma_1 = \mathrm{Re}[\frac{4\pi\omega}{c} \alpha_y^* e^{-i \frac{\omega r}{c}} \sin(\frac{\omega r}{c}) \cos^4 \Theta] \tag{C-30}$$

$$\sigma_2 = \mathrm{Re}[\frac{4\pi\omega}{c} \alpha_z^* e^{-i \frac{\omega r}{c}} \sin(\frac{\omega r}{c}) \sin^4 \Theta] \tag{C-31}$$

$$\sigma_3 = \mathrm{Re}[\frac{4\pi\omega}{c}(\alpha_y^* + \alpha_z^*) e^{-i \frac{\omega r}{c}} \sin(\frac{\omega r}{c}) \sin^2 \Theta \cos^2 \Theta] \tag{C-32}$$

$$\sigma_4 = \mathrm{Re}[\frac{4\pi\omega}{c} i \alpha_y e^{i \frac{\omega r}{c}} \cos(\frac{\omega r}{c}) \cos^2 \Theta] \tag{C-33}$$

$$\sigma_5 = \mathrm{Re}[\frac{4\pi\omega}{c} i \alpha_z e^{i \frac{\omega r}{c}} \cos(\frac{\omega r}{c}) \sin^2 \Theta] . \tag{C-34}$$

The total cross section for p-polarization is the sum of Eqs. (C-30) through (C-34). Upon taking the sum and manipulating properly, the cross section turns out to be

$$\sigma_{\text{total}}\bigg|_{\text{p-pol}} = -\mathrm{Re}\left(\frac{4\pi\omega}{c}\left(e^{-i \frac{\omega r}{c}} \sin(\frac{\omega r}{c})[\alpha_y^* \cos^2 \Theta + \alpha_z^* \sin^2 \Theta] + e^{i \frac{\omega r}{c}} \cos(\frac{\omega r}{c})[i\, \alpha_y \cos^2 \Theta + i\, \alpha_z \sin^2 \Theta]\right)\right) . \tag{C-35}$$

Now, upon letting

$$\alpha = \alpha_y \cos^2\Theta + \alpha_z \sin^2\Theta$$

$$\alpha^* = \alpha_y^* \cos^2\Theta + \alpha_z^* \sin^2\Theta$$

$$\alpha = \mathrm{Re}\,\alpha + i\,\mathrm{Im}\,\alpha \tag{C-36}$$

$$\alpha^* = \mathrm{Re}\,\alpha - i\,\mathrm{Im}\,\alpha$$

$$\alpha^* - \alpha = -2i\,\mathrm{Im}\,\alpha$$

and using Euler's equation for $e^{\pm ikr}$, Eq. (C-35) becomes

$$\sigma_{total}\Big|_{p\text{-}pol} = -\mathrm{Re}\left(\frac{4\pi\omega}{c}\left(-2i\ \mathrm{Im}\,\alpha\cos\left(\frac{\omega r}{c}\right)\sin\left(\frac{\omega r}{c}\right) + i\ \mathrm{Re}\ \alpha\left[\cos^2\left(\frac{\omega r}{c}\right) - \sin^2\left(\frac{\omega r}{c}\right)\right]\right.\right.$$
$$\left.\left. - \mathrm{Im}\ \alpha\left[\sin^2\left(\frac{\omega r}{c}\right) + \cos^2\left(\frac{\omega r}{c}\right)\right]\right)\right) . \tag{C-37}$$

Taking only the real part and using the relation for α given in Eq. (C-36), the final form of the total cross section for p-polarization is seen to be

$$\sigma_{total}\Big|_{p\text{-}pol} = \frac{4\pi\omega}{c}\,\mathrm{Im}\left(\alpha_y \cos^2\Theta + \alpha_z \sin^2\Theta\right) . \tag{C-38}$$

The total cross sections derived here in Eqs. (C-23) and (C-38) are those given in Chapter II by Eqs. (2-42a) and (2-42b).

VITA

Stephen Webster Kennerly was born on June 30, 1956, in Radford, Virginia. He is the son of Mr. and Mrs. Robert G. Kennerly of Greensboro, North Carolina. He was graduated from Grimsley High School in Greensboro, North Carolina, in June, 1974. He entered Appalachian State University in the Fall of 1974 and received the Bachelor of Science degree in physics in December, 1978. He entered graduate school at The University of Tennessee, Knoxville, in the Fall of 1980 and received the Master of Science degree in December, 1983. He is married to the former Miss Terri Lynn Martin of Raleigh, North Carolina.